Delft University of Technology

Document Version
Final published version

Licence
CC BY-NC-ND

Citation (APA)
Gu, C., Hu, X., Yan, X., Chen, W., Chen, J., Lu, K., Wang, T., Zhang, G., & Fan, J. (2025). Interconnection mechanism and strengthening behavior of nano-silver sintered joints for silicon carbide power module packaging: A combined EBSD and nanoindentation study. *Journal of Materials Research and Technology*, *38*, 619-636. https://doi.org/10.1016/j.jmrt.2025.07.135

Important note
To cite this publication, please use the final published version (if applicable).
Please check the document version above.

Copyright
In case the licence states “Dutch Copyright Act (Article 25fa)”, this publication was made available Green Open Access via the TU Delft Institutional Repository pursuant to Dutch Copyright Act (Article 25fa, the Taverne amendment). This provision does not affect copyright ownership.
Unless copyright is transferred by contract or statute, it remains with the copyright holder.

Sharing and reuse
Other than for strictly personal use, it is not permitted to download, forward or distribute the text or part of it, without the consent of the author(s) and/or copyright holder(s), unless the work is under an open content license such as Creative Commons.

Takedown policy
Please contact us and provide details if you believe this document breaches copyrights.
We will remove access to the work immediately and investigate your claim.

This work is downloaded from Delft University of Technology.

Journal of Materials Research and Technology 38 (2025) 619–636

Contents lists available at ScienceDirect

Journal of Materials Research and Technology

journal homepage: www.elsevier.com/locate/jmrt

Interconnection mechanism and strengthening behavior of nano-silver sintered joints for silicon carbide power module packaging: A combined EBSD and nanoindentation study

Chao Gu [a], Xiao Hu [b], Xuyang Yan [a], Wei Chen [a], Junwei Chen [a], Kai Lu [c], Tao Wang [c], Guoqi Zhang [b], Jiajie Fan [a,b,d,*]

[a] Shanghai Engineering Technology Research Center of SiC Power Device, College of Intelligent Robotics and Advanced Manufacturing, Fudan University, Shanghai, 200433, China
[b] EEMCS Faculty, Delft University of Technology, Delft, 2628, the Netherlands
[c] Suzhou XiZ-Tech Co., Ltd, Suzhou, 215000, China
[d] Research Institute of Fudan University in Ningbo, Ningbo, 315336, China

ARTICLE INFO

Handling editor: M Meyers

Keywords:
Silver sintering
Power module packaging
Strengthening behavior
Microstructure features
Interconnection mechanism

ABSTRACT

Investigating the interconnection and strengthening mechanisms of die-attach layers is instrumental for advancing die attach process toward low-pressure and, ultimately, pressureless sintering while maintaining reliability. This study compares the microstructure and micromechanical heterogeneity of the pressure-assisted and pressureless regions in SiC die attach to elucidate the interconnection and strengthening mechanisms. Recrystallized grains make up 71.7 % of the pressureless region, markedly lower than the approximately 90 % observed in the pressure-assisted region, resulting in a higher porosity in the former. Evidence of both continuous dynamic recrystallization and discontinuous dynamic recrystallization is identified throughout the sintered layer. Microhardness reveals that the pressureless zone exhibits a hardness of 0.373 GPa, significantly lower than left (0.745 GPa) and right (1.832 GPa) of pressure-assisted region. All three regions share an average grain size of 400 ± 50 nm, and geometrically necessary dislocation density in pressureless zone exceeds that in pressure-assisted areas, neither of which can account for the difference in micromechanical performance. In contrast, the statistically stored dislocation (SSD) densities on the left and right of the pressure-assisted region are approximately 4.74×10^{14} m^{-2} and 2.88×10^{15} m^{-2}, respectively—substantially higher than the 2.88×10^{14} m^{-2} measured in the pressureless region. Collectively, these findings demonstrate that dislocation strengthening, and particularly SSD density, constitutes the dominant strengthening mechanism in silver sintered layers. This work not only provides new insights for enhancing reliability under low-pressure and pressureless sintering but also establishes a theoretical foundation for optimizing sintering material formulations.

1. Introduction

In response to global climate change and the drive for sustainable development, the renewable energy sector, which encompasses electric vehicles and photovoltaic energy storage, has become a primary focus of innovation [1]. To improve power density and energy conversion efficiency, wide bandgap and ultra-wide bandgap semiconductors have been developed. These semiconductors offer thermal conductivity and bandgap widths nearly three times greater than those of conventional silicon devices, which enables reliable operation in extreme environments [2]. The choice of packaging material is crucial for ensuring reliable device operation. However, conventional solder has notable limitations, including a lower melting point, a poor thermal expansion match with the SiC die, and lower thermal conductivity, all of which pose reliability challenges in high-frequency switching applications [3]. The development of advanced sintering techniques, such as nano-silver sintering, offers a solution to these reliability issues by enhancing the durability of die interconnect layers in harsh environments [4–6].

Today, pressure-assisted silver sintering has become a mainstream,

* Corresponding author. Shanghai Engineering Technology Research Center of SiC Power Device, College of Intelligent Robotics and Advanced Manufacturing, Fudan University, Shanghai, 200433, China.
E-mail address: jiajie_fan@fudan.edu.cn (J. Fan).

https://doi.org/10.1016/j.jmrt.2025.07.135
Received 1 June 2025; Received in revised form 13 July 2025; Accepted 14 July 2025
Available online 19 July 2025
2238-7854/© 2025 The Authors. Published by Elsevier B.V. This is an open access article under the CC BY-NC-ND license (http://creativecommons.org/licenses/by-nc-nd/4.0/).

mass-production-ready silicon carbide die interconnect process in industry. However, this method places significant demands on the structural integrity of the sintered material along the Z-direction. Moreover, applying pressure at high temperatures risks damaging the SiC [7]. Currently, pressure-assisted sintering mainly utilizes graphite sheets as a buffer layer to reduce the pressure impact on the dies, which inevitably increases process complexity. To reduce or even prevent die damage caused by packaging, low-pressure and low-temperature sintering processes, along with pressureless sintering, have become important areas of research [8,9]. However, these interconnection processes, which are characterized by a low sintering driving force, can limit the mechanical properties of the sintered layer, leading to process instability. Thus, exploring the interconnection and strengthening mechanisms of silver sintering processes provides a theoretical foundation for advancing low-temperature, low-pressure, and pressureless sintering techniques.

Existing studies generally agree that the interconnection mechanism of silver nanoparticles is mainly governed by diffusion [10–12]. Research via transmission electron microscopy has shown that surface diffusion dominates at temperatures between 160 °C and 250 °C. As the temperature increases to 300°C-350 °C, volume diffusion becomes the predominant mechanism. Additionally, a positive correlation has been observed between sintering strength and the square of the ratio of neck size to Ag particle size. To differentiate from the sintering mechanism of spherical, isotropic silver nanoparticles, some studies have investigated the anisotropic sintering behavior by preparing triangular silver nanosheets, which were found to form through diffusion facilitated by a bridging effect [11]. In low-temperature sintering processes involving micron and sub-micron silver, curvature studies revealed that diffusion remains the primary mechanism [12]. Alongside experimental findings, molecular dynamics simulations have shown that the sintering process is predominantly governed by a diffusion-based plastic mechanism. Studies have also shown that necked grains tend to tilt and rotate to minimize crystal misorientation [13]. Historically, research into strengthening mechanisms has focused not only on sintering necks but has also utilized molecular dynamics simulations to examine the sintering and melting behaviors of silver nanoparticles. These studies suggest that slip and dislocation mechanisms at high temperatures play a crucial role in strengthening the silver-sintered layer [14,15]. In conclusion, current research on silver sintering mechanisms has primarily focused on the necking of silver particles observed under scanning electron microscopy and on diffusion processes visualized through transmission electron microscopy. Simulations also reveal that grains at the sintering necks tend to tilt and rotate to minimize crystal misorientation [13], which displays typical characteristics of recrystallization. To date, no experimental studies have directly validated the interconnection mechanisms in sintered silver joints.

Furthermore, research on the strengthening mechanisms of nano-silver sintered layers is limited and has primarily focused on sintering morphology, including the dimensions of sintering necks and their impact on mechanical properties [14]. Studies on dislocation strengthening have mainly relied on molecular dynamics simulations [14] and experimental validation of these strengthening mechanisms within the sintered layer is still lacking. Strengthening mechanisms can be categorized into four main types: dislocation strengthening, grain refinement strengthening, solid solution strengthening, and precipitation strengthening [16]. In the absence of solid solution atoms within the sintered material, solid solution strengthening has minimal impact. Additionally, the lack of precipitate phases in the sintered layer suggests that precipitation strengthening is not a primary mechanism. Grain refinement, however, is a significant strengthening mechanism that warrants consideration in such investigations. Dislocation strengthening also plays a critical role and is mainly influenced by geometrically necessary dislocation (GND) density and statistically stored dislocation (SSD) density [17]. The strengthening behaviors of dislocation densities differ, with GND mainly contributing to strengthening near grain boundaries and twin boundaries, while SSD, which is mainly distributed within the grains, plays a strengthening role inside the grains [18].

In summary, current research lacks experimental validation from a microscopic perspective in the exploration of interconnection and strengthening mechanisms. To address this gap, we performed detailed microstructure characterization and micromechanical testing. According to microstructure characterization and micromechanical property testing, this research provides essential data to support the advancement of pressure-assisted sintering towards pressureless sintering, as well as a theoretical foundation for improving the stability of pressureless sintered materials in industrial applications.

This study mainly employs electron backscatter diffraction (EBSD) and nanoindentation techniques to compare the recrystallization fraction, recrystallization type, texture characteristics, GND, and SSD in the sintered layer. Additionally, it compares the micromechanical properties, including hardness and yield strength. The study then explores the interconnection and strengthening mechanisms of the sintered layer by correlating microstructural features with mechanical properties.

2. Experiment

2.1. Materials and method

The test SiC die used in this study was a 1200 V power die manufactured by SICHAIN, identified as SG2M014120B, with dimensions of 4.8 mm × 6.3 mm × 0.2 mm. The backside of the SiC die was metalized with a 1 μm thick layer of Ti/Ni/Ag, while the top metallization layer consisted of Ni/Pd/Au with a thickness of 4 μm. The substrate, supplied by Ferrotec, was fabricated using the active metal brazing (AMB) technology. As shown in Fig. 1(a), the AMB structure featured a sandwich design consisting of Cu/Ceramic/Cu, with the upper and lower copper layers each having a thickness of 0.5 mm, and the ceramic interlayer measuring 0.32 mm. To enhance the reliability of the silver interconnect, a 0.6-μm-thick silver layer was electroplated onto the upper copper layer of the AMB ceramic substrate. For the sintering experiments, a commercially available nano-silver paste, ALPHA ARGOMAX 2020 PASTE, was used, supplied by MacDermid Alpha (Waterbury, CT, USA). Fig. 1(f) shows the particle size of the silver paste before sintering. Statistical analysis reveals that the particle diameter before sintering is approximately 292 nm ± 32 nm. The viscosity at 25 °C is approximately 34 Pa s, and the specific gravity is 3.3 g/cm^3.

As illustrated in Fig. 1(a)–(d), the sintering experiment consisted of four main processes: material preparation, printing, pre-drying, and sintering. A stencil with a thickness of 100 μm was used to ensure the sintered interconnection layer reached approximately 20 μm in thickness. The printing experiments were conducted using the YAMAHA YCP10 fully automatic printing machine. During printing, the blade contact angle was set to 60°, and the printing speed was configured at 100 mm/s. The pre-drying experiments were performed using the Songling HYD90-2T, with a drying temperature of 130 °C and a drying time of 30 min. The dried samples were then placed in the Datacon 2200evo for hot attach experiments, with the substrate heating temperature set to 135 °C. Subsequently, pressure-assisted sintering experiments were conducted on the assembled sandwich structure (SiC/Ag/AMB) using the Boschman Sinterstar Innovate-F-XL. The sintering process took place in a nitrogen atmosphere at 250 °C, with a pressure of 15 MPa for a duration of 300 s, as shown in Fig. 1(e).

2.2. Microstructure characterization

To characterize the microstructural features of the silver sintered interconnect layer and explore their correlation with mechanical properties, EBSD experiments were conducted in regions exhibiting significant variations in mechanical performance. The samples for microstructural analysis were mounted in a 30-mm diameter metallographic epoxy resin mount, as shown in Fig. 1(g). Polishing was performed using sandpaper with grit sizes ranging from #400 to #4000,

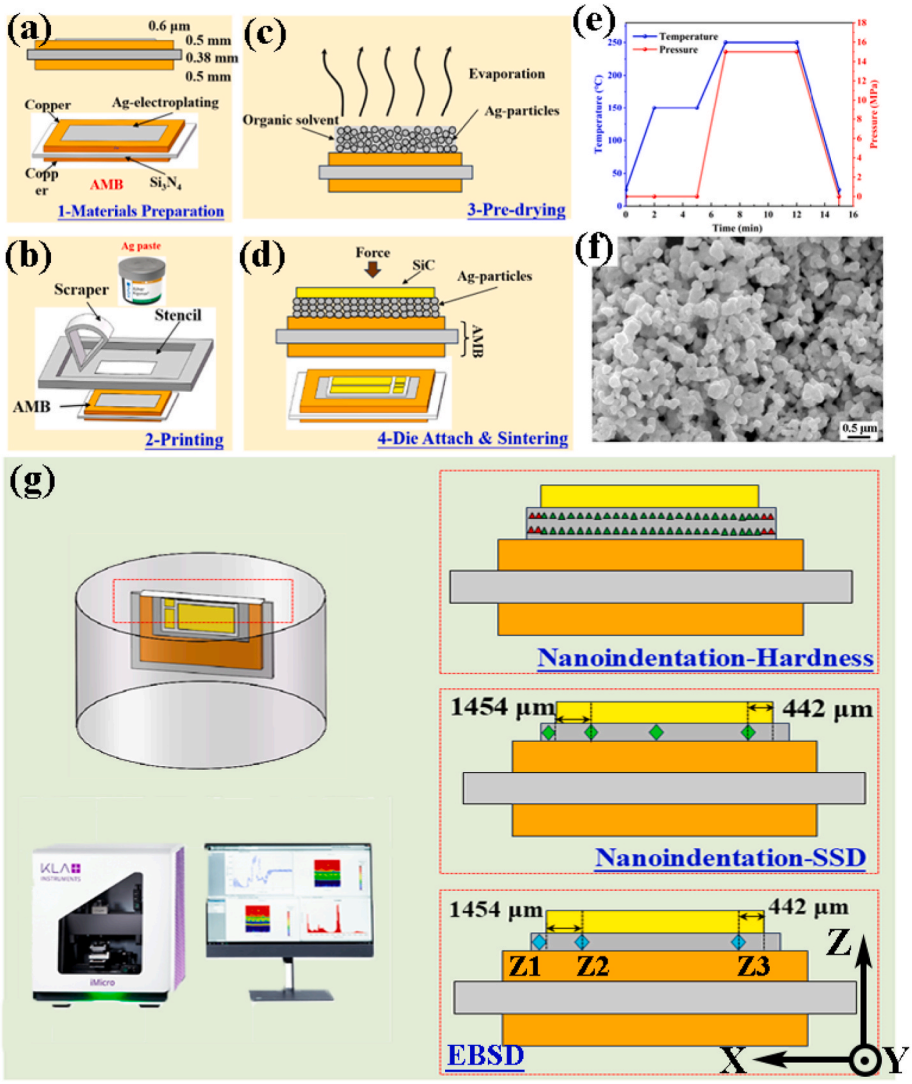

Fig. 1. (a)–(d) Flowchart of the silver sintering process, (e) sintering parameters, (f) the particle size before sintering and (g) schematic showing the positions for nanoindentation and EBSD tests.

followed by diamond spray polishing with particle sizes of 0.5 μm and 2.5 μm. The final cross-section was prepared using a standard Hitachi ion milling machine, model IM4000II, for ion milling. Microstructure characterization of the cross-section was conducted to obtain high-quality orientation data using a Thermo Scientific Apreo 2C device equipped with an EDAX Velocity Super ultrafast EBSD probe. The test was performed at a voltage of 20 kV and an accelerating current of 6.4 nA. The EBSD scan had a step size of 50 nm and covered 400 × 400 pixels. Fig. 1(g) defines the X-Y-Z analysis system for the sample, where X denotes the transverse direction of the sintered layer, Y represents the longitudinal direction of the sintered layer, and Z indicates the thickness direction of the sintered layer. The photographic position, shown in Fig. 1(g), includes three main regions, with the leftmost region being subjected to temperature but not pressure during the sintering process. The remaining two regions were influenced by both temperature and pressure. According to the nanoindentation results, the region with the highest hardness and the region with the lowest hardness were selected for further analysis. To accurately characterize the testing locations, the distances from the measurement points to the SiC edge were marked using an optical microscope, which measured 1454 μm and 442 μm, respectively. Grain size statistics, crystal orientation analysis, grain boundary characterization, and texture analysis were performed using TSL OIM. The proportions of recrystallized grains, deformed grains, and substructures were analyzed using HKL Channel 5 software. The Schmid factor distribution and GND were analyzed using the MATLAB-based MTEX toolbox.

2.3. Nanoindentation test

Nanoindentation experiments were performed using a KLA iNano nanomechanical tester equipped with a diamond Berkovich indenter. To investigate the distribution of mechanical properties across different regions of the interconnect layer and compare the sintered mechanical performance between non-pressurized and pressure-assisted areas, hardness mapping was conducted on the sintered layer. In the nano-indentation mapping tests, owing to the thinness of the sintered layer, experiments were conducted only near the die side and the AMB side, with a 50 μm distance between adjacent test points. The target load was set to 25 mN, the target depth to 500 nm, and the target indentation strain rate to 0.2 s^{-1}, as shown in Fig. 1(g). To calculate SSD, nano-indentation tests were performed at varying depths, with the target depth ranging from 100 nm to 1500 nm and the target load set to 50 mN. The EBSD capture positions were aligned with the locations of the nanoindentation tests to ensure consistent calibration distances and enable the correlation of microstructural features with micromechanical properties.

3. Results

3.1. Microstructure characteristics

3.1.1. Porous and grain features

To accurately correlate the microstructural characteristics of the sintered interconnection layer with its micromechanical properties, relative coordinates are marked after micromechanical performance testing. Microstructural images of the corresponding regions are then captured. Fig. 2 presents the microstructural morphology of different regions in the interconnect layer of the SiC die. Fig. 2(a)–(c) correspond to the positions labeled a–c in the schematic of Fig. 2(d). In the following discussion, the region of artificially created sintered silver overflow, which is not subjected to pressure during sintering, is denoted as Z1. The left and right sides of the pressure-assisted sintering zone are labeled as Z2 and Z3, respectively. Fig. 2(a) shows that Z1 contains a higher quantity of larger pores. In contrast, Z2 and Z3, as illustrated in Fig. 2(b) and (c), exhibit significantly smaller pores and a lower overall pore count, which indicates that pressure plays a critical role in sintering densification. Fig. 2(e) and (f) summarize the porosity, pore count, and pore area across the three regions. As shown, the porosity in Z1 reaches 18.14 % and approaches the 20 % acceptance threshold commonly seen in industrial applications. Additionally, the pore area shows a distinctly heterogeneous distribution, with most pores ranging between 0 and 0.5 μm^2, while the maximum pore area reaches as high as 2.8–3.9 μm^2. In contrast, the porosity in Z2 and Z3 is reduced to 5.14 % and 3.69 %, which represents decreases of 71.7 % and 79.66 %, respectively, compared with the porosity in Z1. The number of pores decreases to 129 and 49, which reflects reductions of 33.5 % and 74.7 %, respectively. Additionally, the pore area distribution in Z2 and Z3 is more consistent than that in Z1, with all distributions falling within the range of 0–0.5 μm^2. In summary, during the sintering process of SiC dies, the porosity in Z1 is approximately 18.14 %, which is significantly higher than in Z2 and Z3, where the porosity ranges from 3.69 % to 5.14 %.

Fig. 3 presents the grain orientation maps for Z1, as well as Z2 and Z3, where high-angle grain boundaries (HAGBs), with a misorientation angle greater than 15°, are marked by black lines. The two types of recrystallized twin boundaries are marked with red lines, with orientation difference angles of 60° and 38.9°, respectively. The colors in the inverse pole figure correspond to different grain orientations, which can be used to determine the crystallographic growth directions. The data indicate that the crystal orientations at all three locations are relatively similar, with a higher prevalence of grains growing along the <001> direction, which is parallel to the Y-axis, and the <101> direction, which is also parallel to the Y-axis. However, no distinct preferred orientation is observed, which suggests that the overall differences in crystal orientation may not be the primary factor contributing to the variations in micro-mechanical properties.

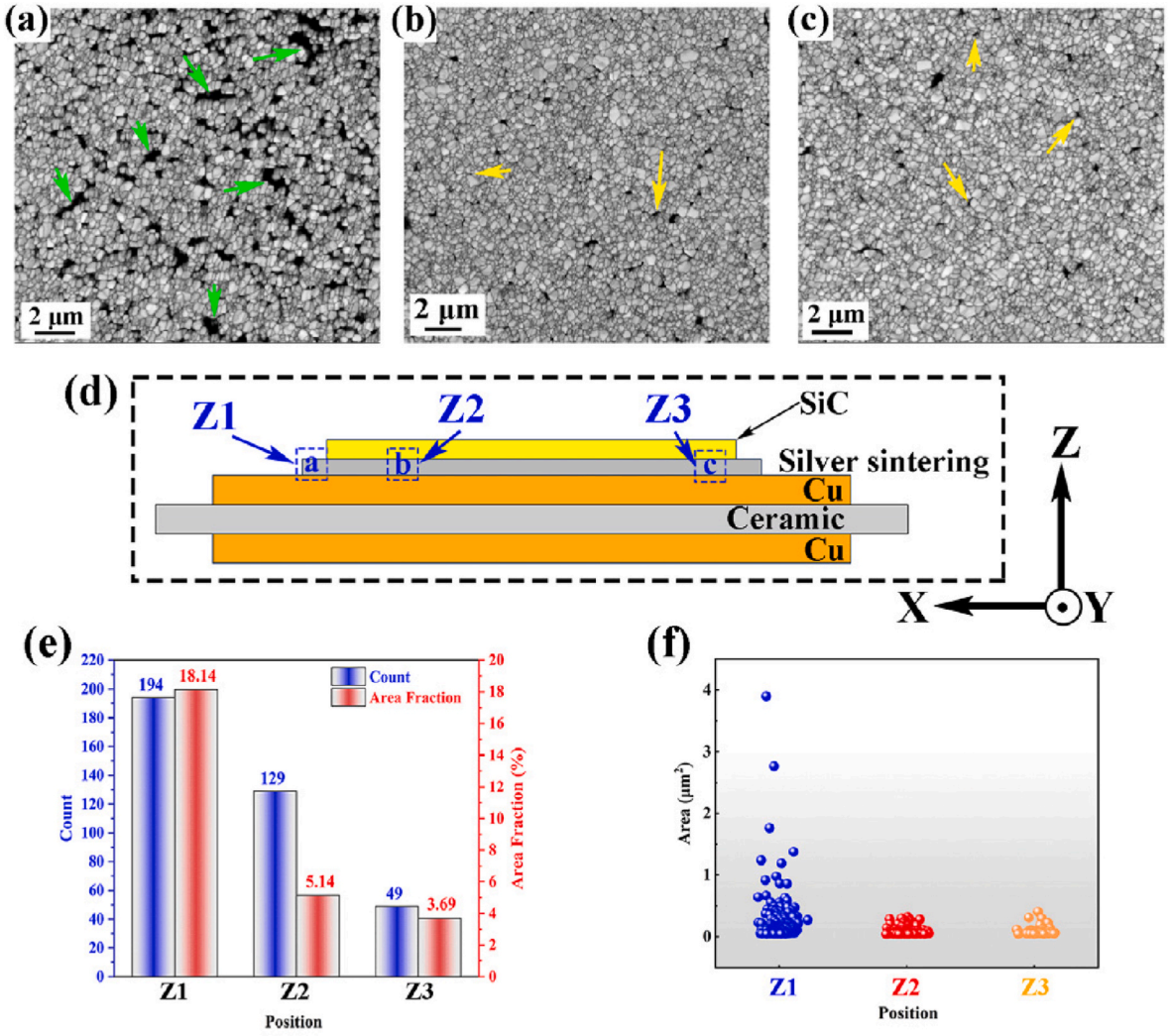

Fig. 2. Microstructural morphology in different regions of the SiC die interconnect layer: (a) Z1, (b) Z2, (c) Z3, (d) position schematic diagram, (e) pore count and (f) area.

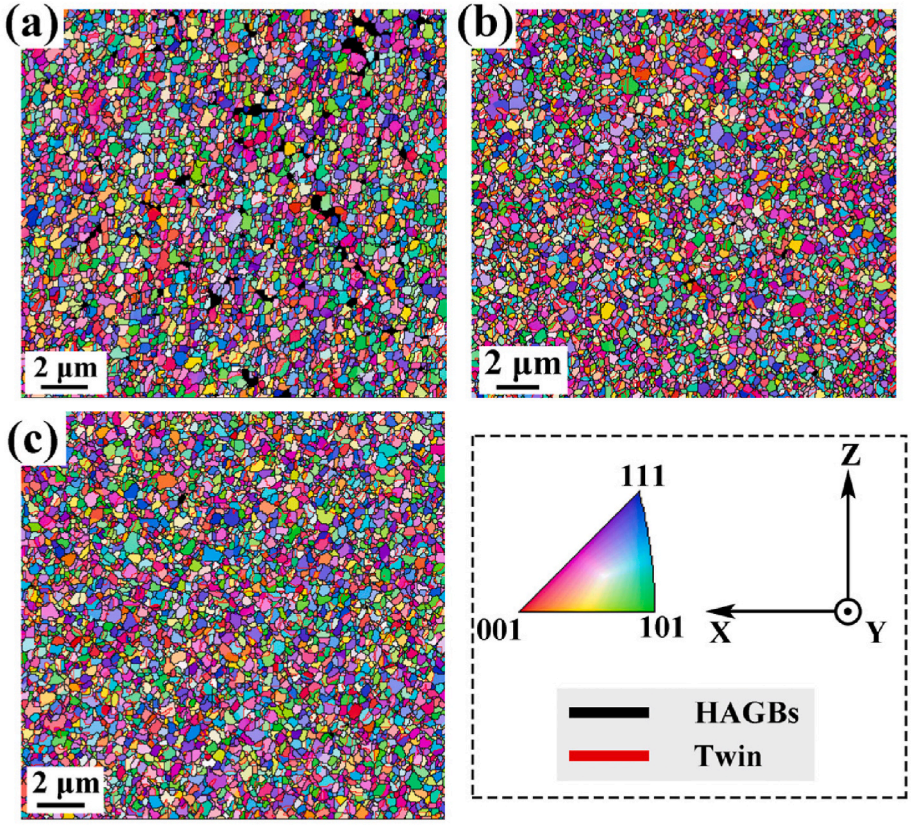

Fig. 3. Inverse pole figure of SiC interconnect layer: (a) Z1, (b) Z2, and (c) Z3.

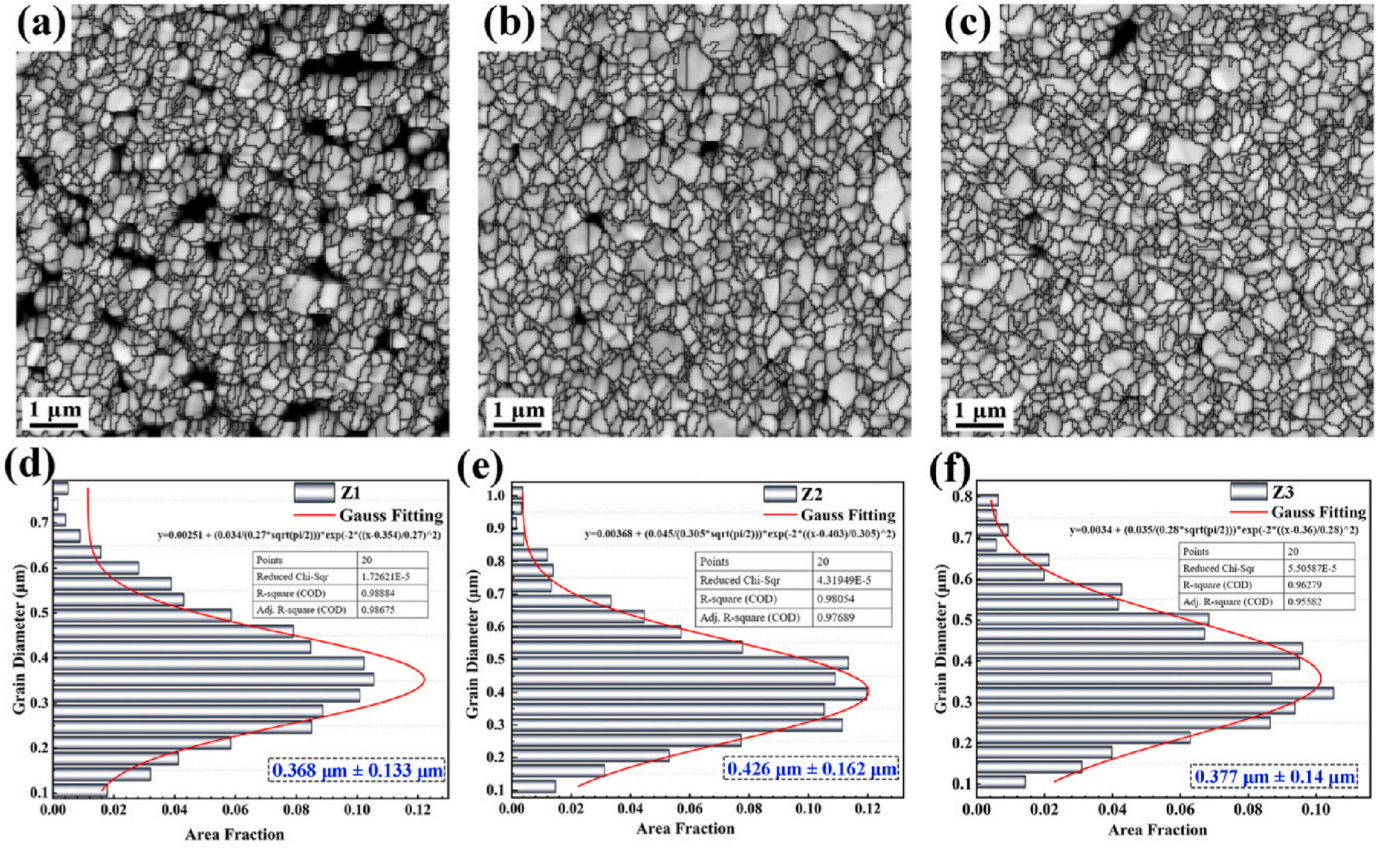

Fig. 4. Grain morphology for (a) Z1, (b) Z2, (c) Z3, and size statistics for (d) Z1, (e) Z2, and (f) Z3.

To quantitatively assess the differences in grain size among the Z1, Z2, and Z3 regions of the sintered layer, EBSD was used to perform a statistical analysis of grain sizes in the three areas, as shown in Fig. 4. Fig. 4(a)–(c) show the grain size distribution for Z1, Z2 and Z3. It can be observed that there is almost no difference among Z1, Z2 and Z3. The grain sizes, indicated in blue font in Fig. 4, are based on statistical results obtained using TSL OIM software, with the analysis conducted under the condition that the influence of twin boundaries is excluded. As illustrated in Fig. 4(d)–(f), the average grain sizes in the Z1, Z2, and Z3 regions are 0.368 μm, 0.426 μm, and 0.377 μm, respectively, with maximum deviations of 0.133 μm, 0.162 μm, and 0.14 μm. This indicates that the maximum difference in grain size, whether in Z1 or between Z2 and Z3, is only approximately 13.6 %. However, the statistical distribution results reveal that the proportion of grains exceeding 0.7 μm in size is significantly higher in Z2 and Z3 (5.19 % and 2.14 %, respectively) than in Z1 (1 %). This suggests that the application of pressure promotes the coalescence and growth of grains. Additionally, Gaussian fitting is applied to the grain size distribution, with the fitting results and corresponding equations presented in Fig. 4(d)–(f). The R-squared values of the distribution are 0.989, 0.980, and 0.963, which indicate a statistically significant relationship. The fitted mean grain sizes are 0.354 μm, 0.403 μm, and 0.360 μm for Z1, Z2, and Z3, respectively. It suggests that while pressure has a minimal impact on the overall grain size in the sintered regions of the die, it does promote localized grain growth.

In conclusion, during the sintering of SiC dies, pressure significantly affects porosity and promotes localized grain growth, but has a lesser impact on overall crystal orientation and average grain size.

3.1.2. *Recrystallization features*

During the interconnection process, the SiC sintered layer is simultaneously subjected to temperature and pressure, representing a typical thermo-mechanical coupling process. Under this coupling, the interconnection mechanism primarily consists of dynamic recovery and dynamic recrystallization, which directly influences the microstructural evolution and mechanical properties. Therefore, it is crucial to discuss the interconnection mechanism of SiC sintered layers.

Fig. 5 shows the distribution of grain boundaries in the interconnect layer. HAGBs, with an orientation difference angle greater than 15°, are marked with a black line. Low-angle grain boundaries (LAGBs), with an orientation difference angle between 2° and 15°, are marked with a green line. The twin boundaries, which mainly consist of two types of recrystallized twins with orientation difference angles of 60° and 38.9°, are also marked with a red line. Fig. 5(a) represents the region subjected to sintering without applied pressure, which falls under the categories of static recovery and recrystallization. Fig. 5 (b) and (c) depict regions directly beneath the die, which fall under the category of dynamic recrystallization. Fig. 5(d) is a magnified view of the region shown in Fig. 5(b). SiC sintering is a typical plastic deformation process influenced by temperature. During this process, dislocations proliferate and migrate significantly. When the stacking fault energy is relatively high, dislocations can rearrange in an orderly manner through slip and climb mechanisms to form sub-grain boundaries, as indicated by the blue arrows in Fig. 5(d). As plastic deformation progresses, sub-grain boundaries gradually absorb dislocations, leading to an increase in misorientation. When the misorientation exceeds 15°, HAGBs form, which partitions the original large grains. This mechanism of increasing misorientation is a characteristic feature of continuous dynamic recrystallization (CDRX) [19–21]. Lattice rotation typically occurs at grain boundaries, where sub-grains, which are formed by dislocation slip and climb within the grains, undergo rotation as driving forces such as temperature or strain increase. This rotation promotes the formation

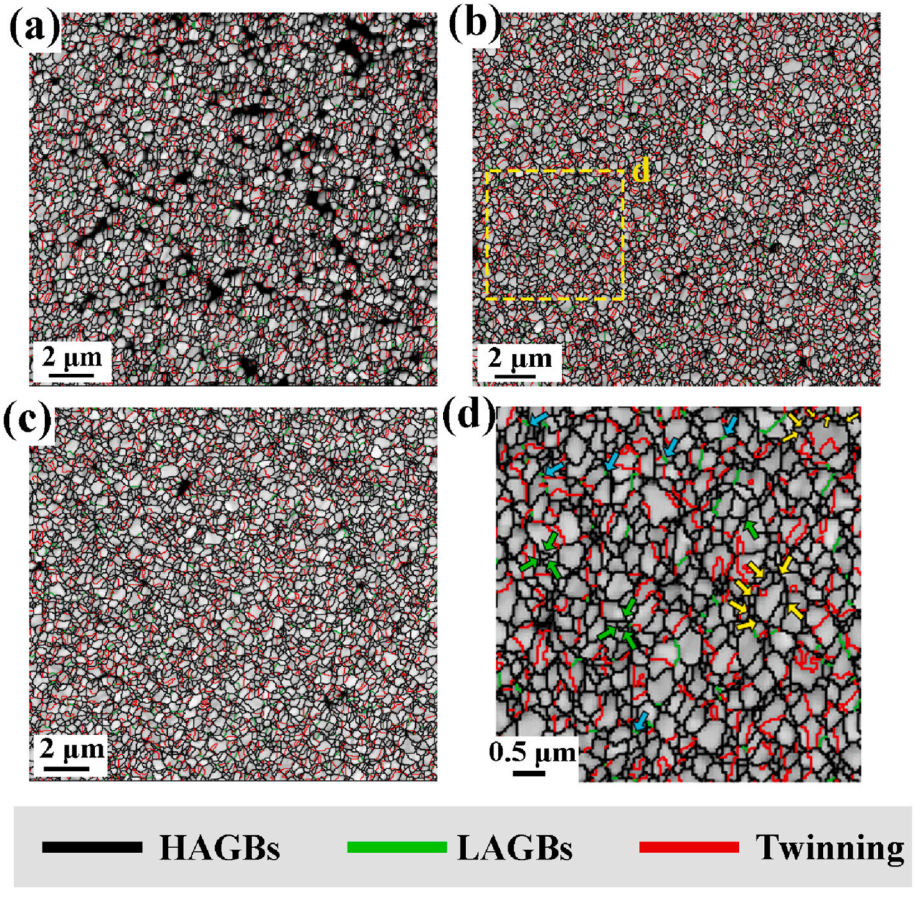

Fig. 5. Distribution of grain boundaries in the interconnect layer of SiC dies: (a) Z1, (b) Z2, (c) Z3 and the (d) localized enlarged view of (b).

of new recrystallized grains. Additionally, typical characteristics of discontinuous dynamic recrystallization (DDRX) [21,22] were observed in the sintered layer of SiC dies. As indicated by the yellow arrows in Fig. 5(d), a cluster of continuous and fine grains is distributed in a "necklace-like" arrangement around a larger grain. This phenomenon is mainly attributed to the accumulation of a significant number of dislocations during the plastic deformation process, which becomes blocked at the grain boundaries. Once the threshold is reached, dynamic recrystallization nuclei form at the grain boundaries and either grow or diminish under the influence of stored energy and interfacial energy. In conclusion, the primary interconnection mechanisms in the interconnect layers are CDRX and DDRX.

Additionally, according to Fig. 5, the grain boundary lengths in the three regions are quantified and summarized in Table 1. The statistics in the table show that all regions have the largest percentage of HAGBs, which range from 80 % to 85 %. LAGBs have the smallest percentage, approximately 2.5 %, while twin boundaries account for around 13 %–15 %. Furthermore, the proportions of HAGBs, LAGBs, and twin boundaries in the three regions exhibit minimal variation, which indicates that, during the sintering process, the impact of pressure on the overall crystal orientation and the quantity of grain boundaries is not particularly significant.

Fig. 6 shows the distribution of the recrystallized fraction in the sintered layer of the SiC die, as determined using Channel 5 software. In the figure, blue grains represent recrystallized grains, yellow grains represent substructured grains, and red grains represent deformed grains. For this study, grains with an average intragranular misorientation of less than 1° are classified as recrystallized grains, grains with misorientations between 1° and 7.5° are classified as substructured grains, and grains with misorientations greater than 7.5° are classified as deformed grains. As seen in Fig. 6(a) and (d), the Z1 region is mainly composed of recrystallized grains, which account for 71.7 % of the total. Substructured grains and deformed grains make up 26.3 % and 2 %, respectively. In contrast, the Z2 and Z3 regions exhibit significantly higher proportions of recrystallized grains, with 91.3 % in Z2 and 89.6 % in Z3. Substructured grains account for 8.04 % and 9.72 %, while deformed grains make up 0.629 % and 0.694 %, respectively. Additionally, Fig. 6 shows that substructured and deformed grains are commonly distributed around the pores. This suggests that, from a macroscopic perspective, pore healing during the sintering process primarily manifests as recrystallization at the microscopic level. In summary, pressure plays a crucial role in the transformation of substructured grains into recrystallized grains during sintering.

In the region of pressure-assisted sintering, the dynamic recrystallization processes in Z2 and Z3 show minimal differences. Sole reliance on the distribution of recrystallized grains to explain the extent of recrystallization may lead to significant errors. Therefore, integrating the grain orientation spread (GOS) map with the recrystallized grain distribution map can improve the reliability of the data. The GOS distribution map is generated by selecting several points within a grain and calculating the average misorientation angle of all selected points to determine the GOS value for that grain [23]. Fig. 7 illustrates the GOS in the interconnect layer, where the white region indicates a small grain internal misorientation, and the red region indicates a large grain internal misorientation. In the Z1 region, the overall grain misorientation is significantly higher than in the Z2 and Z3 regions. Additionally, grains with higher GOS values are predominantly distributed around the pores. According to the statistical results obtained from TSL OIM software, the GOS values for the Z1, Z2, and Z3 regions are 0.230° ± 0.21°, 0.158° ± 0.148°, and 0.11° ± 0.09°, respectively. Fig. 7(d) presents the GOS statistics and Gaussian fitting results for the three regions, with a grain count of approximately 7000 to 9,000, all of which follow a normal distribution (R-squared values of 0.895, 0.95, and 0.92, respectively). Therefore, the data can be considered reliable and accurate. According to the fitting results, the average GOS values for the Z1, Z2, and Z3 regions are 0.1494°, 0.1288°, and 0.092°, respectively. This indicates that the recrystallization degree is lowest in the Z1 region and higher in the Z2 and Z3 regions, with the Z3 region exhibiting the highest degree of recrystallization.

In conclusion, the primary interconnection mechanism is dynamic recrystallization, with the dominant recrystallization types being CDRX and DDRX. The degree of recrystallization is highest in the Z3, followed by the Z2, while the Z1 exhibits the lowest recrystallization degree.

3.1.3. Texture development

To accurately analyze the texture characteristics of the sintered layer in different regions, the orientation distribution functions (ODFs) for Z1, Z2, and Z3 are obtained via EBSD, as shown in Fig. 8(a)–(c), with the component information for all textures summarized in Table 2. Fig. 8(d) presents a typical ideal texture component. As seen in Fig. 8, the texture features of the three regions are partially similar, each containing the deformed textures S and RT Brass. The deformed RT Brass texture in Z1 exhibits the highest intensity, approximately 1.471. Additionally, typical recrystallized textures, such as F, Cube, and $Cube_{ND}$, are observed with an intensity of about 1.3, while the S texture has an intensity of approximately 1.35. Similar to Z1, Z2 also contains Cube, RT Brass, F, and S textures, with intensity values of 1.2, 1.492, 1.3, and 1.185, respectively. Additionally, the Z2 exhibits a copper texture with an intensity of approximately 1.4 and an RT Cube texture with an intensity of around 1.2. In contrast, the Cube texture completely disappears in Z3, while a relatively high intensity (1.377) of the RT Brass texture is still preserved. $Cube_{ND}$, which disappears in Z2, reappears in Z3 with an intensity of 1.236. Furthermore, the Goss texture and shear texture B/ $\overline{B}$ also develop in Z3, with the intensities of S and copper reaching up to 1.377. The volume fraction of the sintered layer texture is statistically summarized in Fig. 8(e). The volume fraction of the deformed texture S is the highest and accounts for 3.1 %, 2.7 %, and 2.7 % in Z1, Z2, and Z3, respectively. The volume fraction of the Cube texture is highest in Z1 (0.9 %) and decreases to 0.7 % in Z2, while Cube is absent in Z3. The combined volume fraction of the remaining recrystallization textures in the three regions is approximately 4 %. Additionally, the shear texture B/ $\overline{B}$ is present in Z3 and accounts for 1.2 %. Furthermore, the total texture volume fractions of Z1, Z2, and Z3 are 8 %, 8.8 %, and 9.6 %, respectively, which indicates that the sintered layer of the SiC die does not exhibit a significant crystal-preferred orientation.

3.2. Micro-mechanical properties

3.2.1. Hardness distribution

Nanoindentation is currently a crucial technique for characterizing micro-mechanical properties in the semiconductor field. Fig. 9(a) presents a schematic of the nanoindentation experiment, highlighting the

Table 1
Statistical results of grain boundaries in different regions.

	Z1		Z2		Z3	
	Length/μm	Proportion/%	Length/μm	Proportion/%	Length/μm	Proportion/%
HAGBs	2860	84.5	4170	82.2	3220	84.6
LAGBs	79.69	2.4	124.9	2.5	92.84	2.4
Twinning	444.3	13.1	776.43	15.3	492.36	13

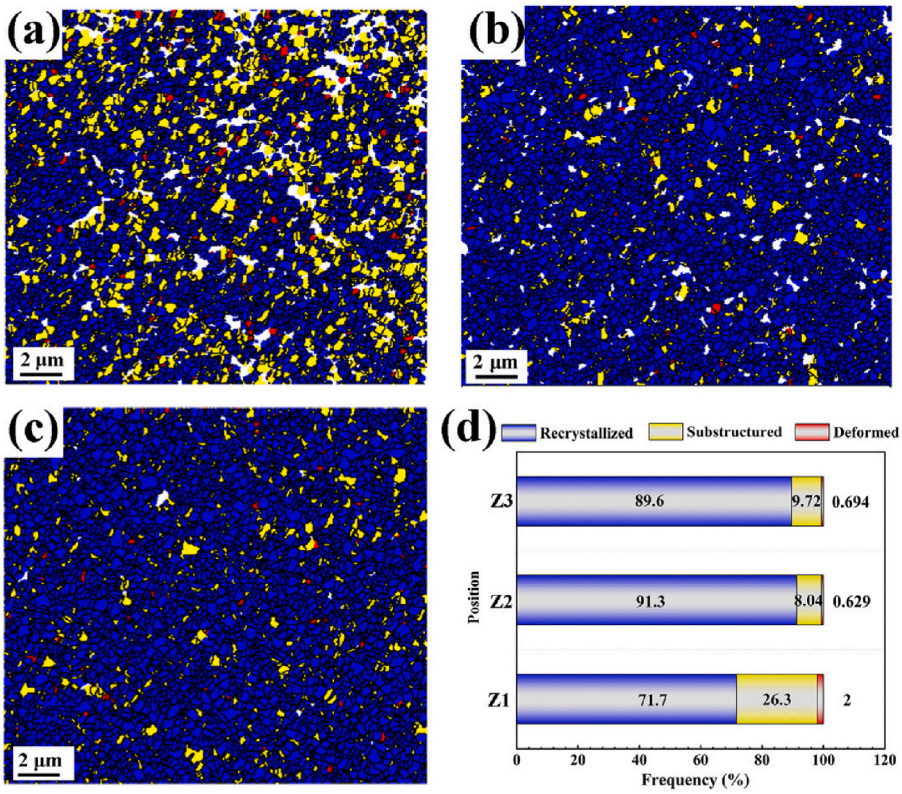

Fig. 6. Distribution of recrystallized grains in the interconnect layer (a) Z1, (b) Z2, (c) Z3, and (d) statistical chart.

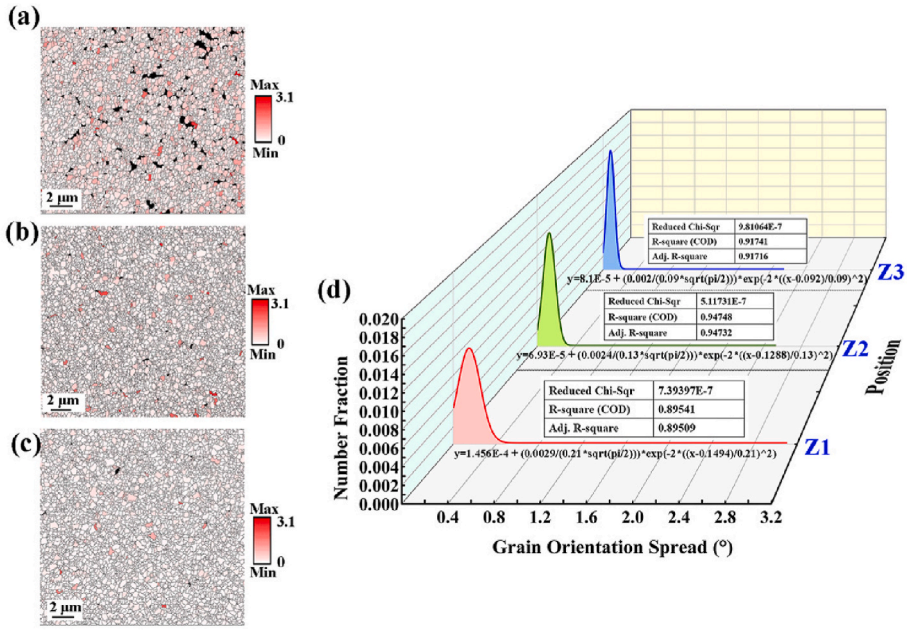

Fig. 7. Grain orientation spread in the interconnect layer: (a) Z1, (b) Z2, (c) Z3, and (d) statistical chart.

key parameters. The results of the nanoindentation experiments are primarily presented as load-displacement (P-h) curves, as shown in the first quadrant of Fig. 9(b). By connecting the nanoindentation schematic with the P-h curve, key information about the sample indentation can be obtained to calculate micro-mechanical parameters, where h_{max} represents the maximum indentation depth (subsequently referred to as h_m), h_c is the contact depth, and A_m is the projected area of the maximum contact region in the vertical direction. h_r represents the distance from the indenter tip to the initial surface of the sample after unloading. Based on the P-h curve, the nanoindentation process can be divided into three stages: the loading curve, the holding curve, and the unloading curve [25]. The data presented in the figure. indicate that during the loading phase, the P-h curve follows a quadratic function ($P = Ch^2$), suggesting that the rate of load increase accelerates with increasing penetration depth. Upon reaching the maximum load penetration depth, the system enters a load-holding stage. Subsequently, as the indenter is

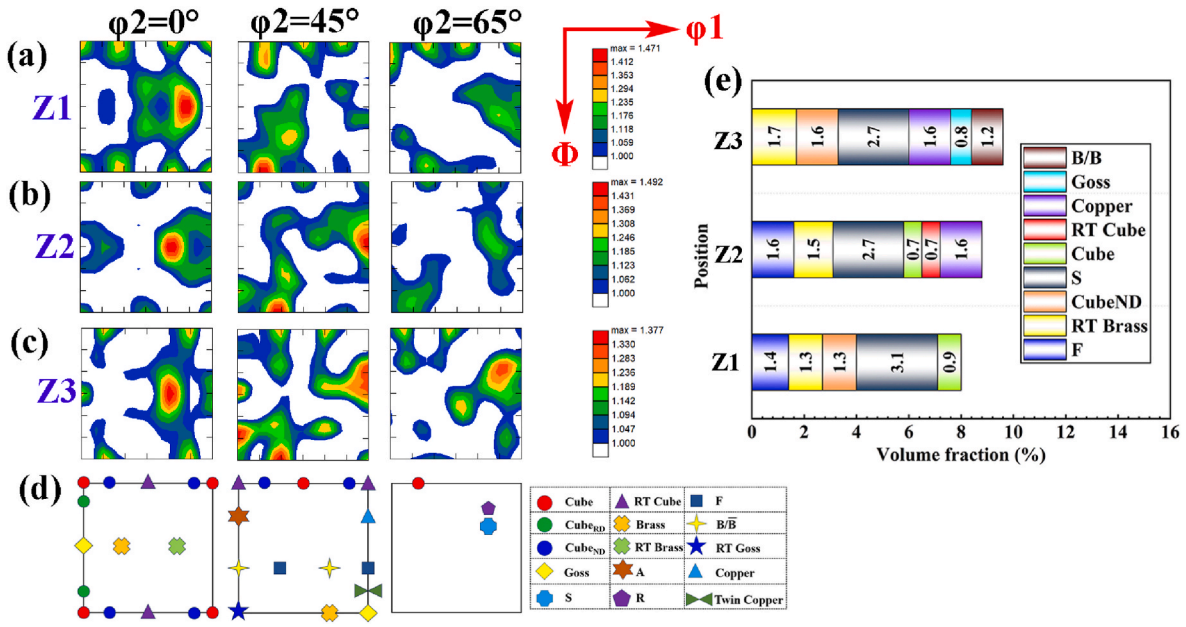

Fig. 8. ODFs distribution in the interconnect sintered layer of SiC die: (a) Z1, (b) Z2, (c) Z3, and (d) ideal texture component, and (e) the texture volume fraction.

Table 2
Miller Indices and Euler Angles of main texture orientations [24].

Designation	Miller Indices {*hkl*}<uvw>	Euler Angles (°)		
		φ1	Φ	φ2
F	{111}<112>	30/90	55	45
B/ $\bar{B}$	{111}<110>	0/60	54.7	45
RT brass	{110}<111>	35	90	45
		55	45	0
RT cube	{001}<110>	45	0/90	0
Cube$_{ND}$	{001}<310>	18.4/71.6	0	0
S	{213}<634>	58.98	37.70	63.43
Cube	{001}<100>	0/90	0/90	0/90
Copper	{112}<111>	90	35	45
Goss	{011}<100>	0	45	0/90

retracted, the load gradually decreases, transitioning into the unloading stage [26]. The figure indicates that the total work during the application of load can be divided into elastic work (W_e) and plastic work (W_p).

Based on the classical mechanics approach and plastic deformation theory by Oliver and Pharr [27], the analysis of the P-h curve data allows for the discussion of the mechanical parameters, such as hardness and equivalent elastic modulus, according to Eqs (1)–(3) [28,29]:

$$H = \frac{P_{max}}{A_m} \tag{1}$$

$$A_m \approx 24.56 h_c^{\,2} \tag{2}$$

$$S = \left.\frac{dP}{dh}\right|_{h_m} \tag{3}$$

where H represents hardness, P_{max} denotes the maximum applied load, E^* is the equivalent elastic modulus. The slope at the upper end of the unloading curve, denoted as S, can be calculated in conjunction with Fig. 9(b) and Eq. (3). The contact depth, denoted as h_c, can be calculated by Eq. (4) [28]:

$$h_c = h_{max} - \varepsilon \frac{P_{max}}{S} \tag{4}$$

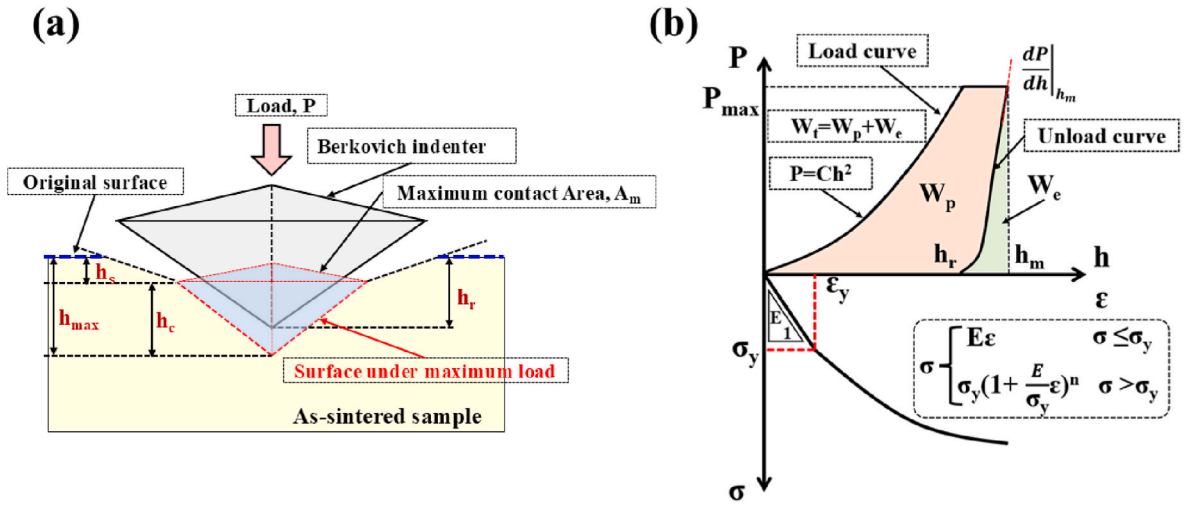

Fig. 9. (a) Schematic of nanoindentation, (b) schematic of the nanoindentation load–displacement curve and stress–strain curve.

where ε is a constant (for a diamond Berkovich indenter, $\varepsilon = 0.75$). The maximum indentation depth (h_{max}) can be directly obtained from the test results and the P-h curve.

Additionally, the equivalent elastic modulus E^* can be defined based on the elastic modulus and Poisson's ratio of the test samples and the Berkovich indenter, as shown in Eq. (5) [26]:

$$\frac{1}{E^*} = \frac{1-\upsilon^2}{E} + \frac{1-\nu_i^2}{E_i} \tag{5}$$

where E_i and υ_i represent the elastic modulus and Poisson's ratio of the diamond Berkovich indenter, respectively. In this paper, the values for E_i and υ_i are taken as 1140 GPa and 0.07, respectively. Here, E and υ represent the elastic modulus and Poisson's ratio of the test samples. The elastic modulus (E) for different regions was determined based on the results of nanoindentation experiments, with a Poisson's ratio of 0.37 for silver [9].

In summary, nanoindentation is an effective technique for determining the mechanical parameters of materials through numerical calculations.

3.2.2. Nanoindentation stress-strain curve

To investigate the differences in the micro-mechanical properties of the sintered layer, nanoindentation experiments were conducted at 50 μm intervals along the X direction. Owing to the thin nature of the sintered layer, nanoindentation is performed in two distinct regions: one near the SiC side and the other near AMB side. According to the results obtained from the P–h curves, the hardness is calculated using Eqs. (1), (2) and (5), and subsequently visualized as a contour plot, as shown in Fig. 10(a). The top and bottom regions marked in Fig. 10(a), as well as the left, center, and right positions on both the top and bottom sides, along with the non-pressurized area, are extracted and plotted as box plots with Gaussian fitting, as shown in Fig. 10(b). The hardness of the sintered layer near the AMB side and the SiC side are approximately 1.089 ± 0.31 GPa and 1.027 ± 0.25 GPa, respectively, with the hardness near the AMB side being about 6 % higher than near the SiC side. This is primarily due to the close coefficient of thermal expansion (CTE) between silver in the die attach layer (18.9 ppm/K) and copper on the AMB (16.5 ppm/K), in contrast to the significant difference from SiC (5.1 ppm/K). During the cooling process, SiC hinders the shrinkage of the sintered layer, making it difficult for pores to heal, which is manifested as lower hardness. In the sintered area near the SiC side, the hardness is generally lower on the left side (around 0.95 ± 0.26 GPa), highest in the center (around 1.13 ± 0.21 GPa), and around 1.03 ± 0.25 GPa on the right side. The hardness on the left side is approximately 16 % lower than in the center and 8 % lower than on the right side. In the region near the AMB side, the hardness values are approximately 0.96 ± 0.28 GPa on the left, 1.18 ± 0.21 GPa in the center, and 1.21 ± 0.37 GPa on the right. Notably, the hardness on the left is approximately 20.7 % lower than that on the right. In regions not subjected to external pressure, the hardness shows good consistency but is generally low and measures approximately 0.38 ± 0.03 GPa. According to these results, the hardness of the sintered layer under pressure is approximately three times higher than that of the sintered layer without pressure. This provides a data foundation for the subsequent comparative investigation of the strengthening mechanisms in the pressure-assisted and non-pressurized regions. Additionally, the variations in mechanical properties within the pressure-assisted area further support the need for research into its strengthening mechanisms.

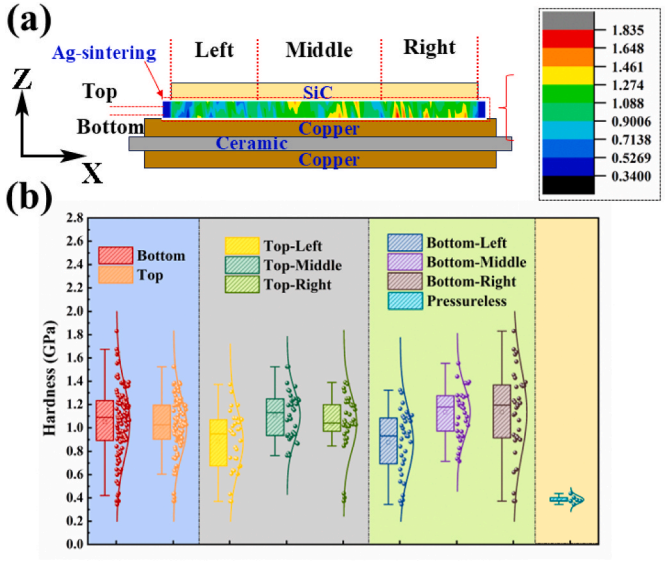

Fig. 10. (a) Hardness distribution of die interconnection layers and (b) statistical graphs.

In conclusion, the hardness in the pressure-assisted region is approximately three times greater than in the non-pressurized region. Additionally, the hardness near the AMB side is approximately 6 % higher than near the SiC side, while the hardness in the left region of the sintered layer is 8 %–20.7 % lower than that in the middle and right sides.

3.2.3. P-h curve transformed to stress-strain curve theory

The stress-strain curve is another key indicator for studying the mechanical behavior of materials. It not only describes material properties such as yield strength and elastic modulus but also serves as a direct reference for understanding and predicting these properties. In addition to providing information on hardness and SSD, nanoindentation enables the numerical calculation of yield strength and the generation of stress–strain curves [26]. The fourth quadrant Fig. 9(b) shows a typical stress–strain curve along with a mathematical model, as represented in Eq. (6). The figure highlights that the boundary between the elastic and plastic deformation stages occurs at the yield strength. In the elastic deformation stage, a linear region can be defined based on the elastic modulus and yield strength of the material. In the plastic deformation stage, the plastic deformation region is characterized using Eq. (6) [30]:

$$\sigma = \begin{cases} E\varepsilon & \sigma \le \sigma_y \\ \sigma_y\left(1+\dfrac{E}{\sigma_y}\varepsilon\right)^n & \sigma > \sigma_y \end{cases} \tag{6}$$

where ε represents strain, and n denotes the strain hardening exponent (usually 0.1–0.5 for metallic materials) [31].

Building on previous research, we improved the method for converting the P-h curves obtained from nanoindentation experiments into stress-strain curves, as illustrated in the flowchart in Fig. 11. Converting P-h curves to stress-strain curves requires ensuring that nanoindentation is performed on homogeneous material regions, avoiding pores. In porous sintered materials, excessive indentation depth should be avoided to prevent pore collapse or indenter contact with internal pores. The maximum indentation depth used in this study for P-h to stress-strain conversion is only 500 nm, and a Berkovich indenter (rather than a spherical indenter) is employed to effectively reduce the occurrence of pore collapse due to its sharp tip geometry. If a significant increase in loading curvature is observed during indentation testing, the indentation data are deemed unreliable and the test needs to be repeated. It is clear from the previous formulation that the P-h curve can be fitted to a quadratic function during the applied load stage and the coefficients C of the function can be obtained. h_m, h_r, and P_m can be acquired directly from the P-h curve. W_p/W_t can be calculated from the integral area of the P-h curve enclosed with the X-axis, and S can be obtained from the slope of the curve at the maximum indentation depth. The maximum indentation area can be obtained by bringing the

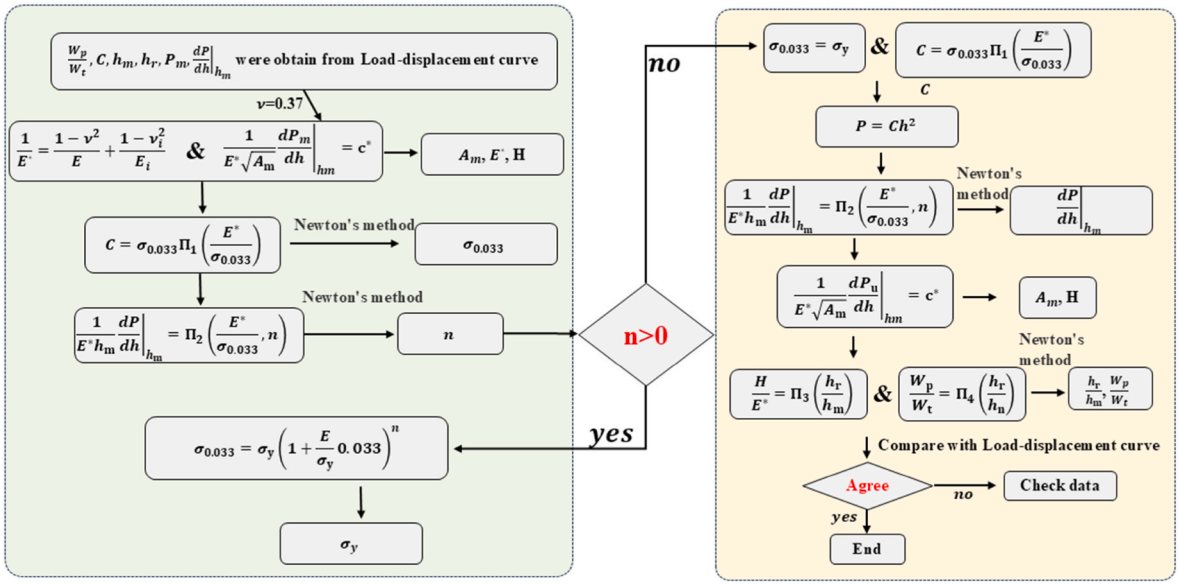

Fig. 11. Flowchart for converting P–h curves to stress–strain curves.

equivalent elasticity module obtained from Eq. (5) into Eq. (7) [31]:

$$\frac{1}{E^*\sqrt{A_m}}\frac{dP_m}{dh}\bigg|_{h_m} = c^* \tag{7}$$

where c^* is a constant. For diamond Berkovich, c^* takes 1.167 when the deformation is in the linear-elastic stage, and 1.237 when it is in the elastic-plastic deformation stage.

Substitution of the parameters C and E^* into Eq. (8) and application of Newton's iterative method yields the parameter $\sigma_{0.033}$, which serves as a normalized, dimensionless function related to the strain hardening index [31]:

$$\frac{C}{\sigma_{0.033}} = \prod_1\left(\frac{E^*}{\sigma_{0.033}}\right) = -1.131\left[\ln\left(\frac{E^*}{\sigma_{0.033}}\right)\right]^3 + 13.635\left[\ln\left(\frac{E^*}{\sigma_{0.033}}\right)\right]^2 - 30.594\left[\ln\left(\frac{E^*}{\sigma_{0.033}}\right)\right] + 29.267 \tag{8}$$

where Π_1 is a dimensionless function, C is the loading curvature. Then, the calculated value of $\sigma_{0.033}$ is substituted into Eq. (9), and Newton's iterative method is applied to determine the strain hardening index n:

$$\frac{1}{E^*h_m}\frac{dP}{dh}\bigg|_{h_m} = \prod_2\left(\frac{E^*}{\sigma_{0.033}}, n\right) = (-1.4n^3 + 0.78n^2 + 0.16n - 0.068)\left[\ln\left(\frac{E^*}{\sigma_{0.033}}\right)\right]^3 + (17.93n^3 - 9.22n^2 - 2.38n + 0.863)\left[\ln\left(\frac{E^*}{\sigma_{0.033}}\right)\right]^2 + (-80n^3 + 40.56n^2 + 9n - 2.545)\left[\ln\left(\frac{E^*}{\sigma_{0.033}}\right)\right] + (122.65n^3 - 63.9n^2 - 9.59n + 6.2) \tag{9}$$

where Π_2 is a dimensionless function, $\frac{dP}{dh}\Big|_{h_m}$ is the unloading slope at the maximum indentation depth. When $n > 0$, the yield strength σ_y can be calculated using Eq. (10) [31]:

$$\sigma_{0.033} = \sigma_y\left(1 + \frac{E}{\sigma_y} \times 0.033\right)^n \tag{10}$$

A piecewise function representing the stress–strain behavior across both the elastic and elastoplastic regions is obtained by substituting σ_y and n into Eq. (6), which allows for the construction of the stress–strain curve.

When $n < 0$, it is necessary to set $n = 0$. Under this assumption, $\sigma_{0.033}$ is considered equivalent to σ_y and this value is substituted into Eq. (8) to determine the parameter C of the P–h curve. The slope of the P–h curve at the maximum indentation depth can be calculated by concurrently applying Eq. (9). The projected area and hardness at the maximum indentation depth are derived using Eq. (7). These values are then substituted into Eqs. (11) and (12), and by employing Newton's iteration method, the ratios h_r/h_m and W_p/W_t in the P-h curve can be obtained [31]:

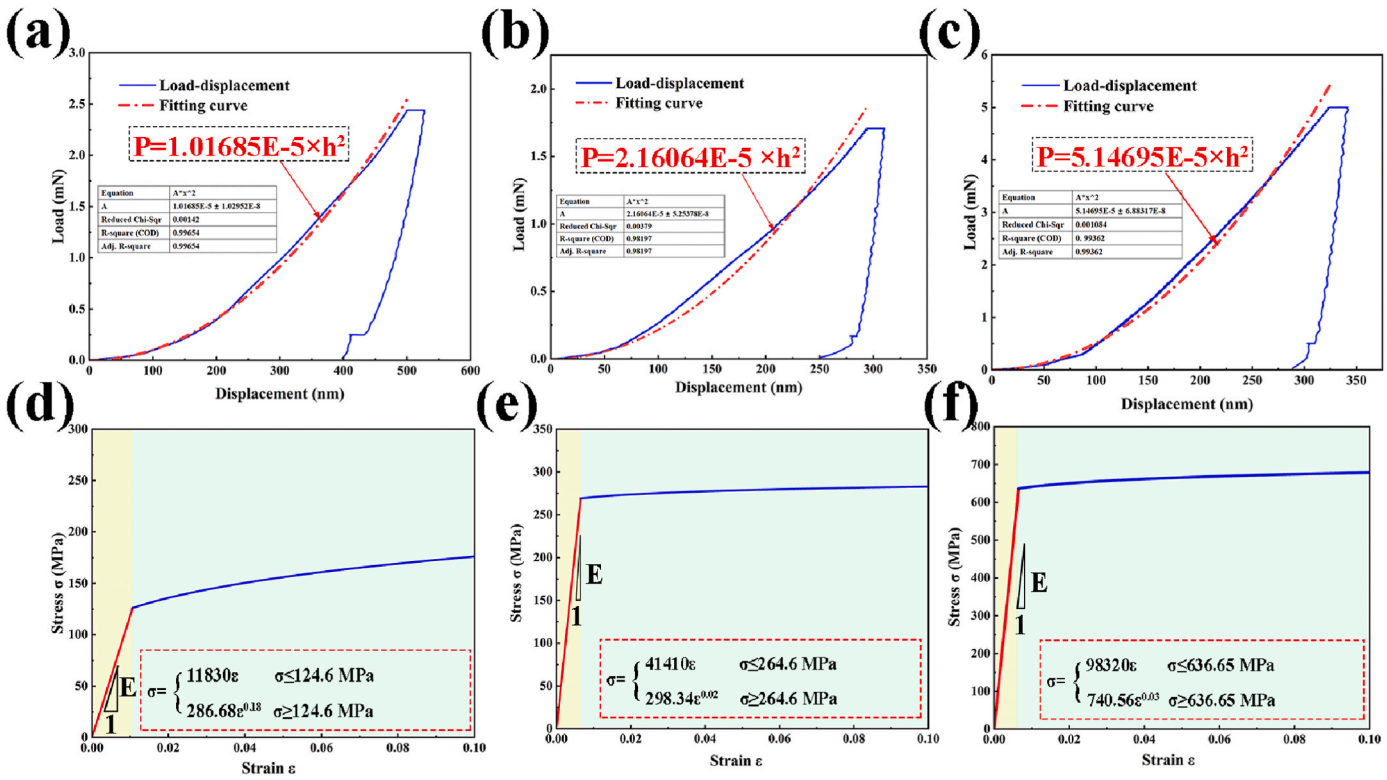

Fig. 12. P-h curves and stress-strain curves of SiC interconnection layers: (a)(d) Z1, (b)(e) Z2, and (c)(f) Z3.

Table 3
Parameters for the transformation of P-h curves into stress-strain curves.

	C (GPa)	H (GPa)	E^* (GPa)	A_m (nm^2)	dP_{max}/dh (N/m)	$\sigma_{0.033}$ (GPa)	n	σ_y (GPa)
Pressureless	10.17	0.373	13.54	5.48×10^{-12}	39207	0.162	0.18	0.1246
Left	21.61	0.745	46.08	6.24×10^{-12}	93037	0.276	0.02	0.2646
Right	51.47	1.832	103.61	3.10×10^{-12}	225756	0.672	0.03	0.6365

$$\frac{H}{E^*} = \prod_3\left(\frac{h_r}{h_m}\right) \approx 0.27\left(0.995 - \frac{h_r}{h_m}\right)^{1.1142735} \tag{11}$$

$$\frac{W_p}{W_t} = \prod_4\left(\frac{h_r}{h_m}\right) = 1.612\left\{1.13 - 1.75\left[-1.493\left(\frac{h_r}{h_m}\right)^{2.535}\right] - 0.0752\left(\frac{h_r}{h_m}\right)^{1.135826}\right\} \tag{12}$$

where Π_3 and Π_4 are dimensionless functions. Finally, the parameters obtained from the reverse analysis are compared with the experimental P–h curve parameters. If a good match is observed, the results can be reported; otherwise, the data will require recalibration.

In summary, nanoindentation experiments offer an effective method for deriving stress–strain curves and corresponding mechanical parameters for test samples through numerical analysis.

3.2.4. Nanoindentation stress-strain curve

To comprehensively investigate the micro-mechanical properties of the sintered layer, three regions with distinctly different hardness levels—Z1, Z2, and Z3—were selected for analysis. This approach aims to explore variations in yield strength by providing valuable data to support the subsequent study of strengthening mechanisms. The hardness values for Z1, Z2, and Z3 are 0.373 GPa, 0.745 GPa, and 1.832 GPa, respectively. The P–h curves from each region can be transformed into stress–strain curves, using Eqs. (6)–(12), as outlined in Fig. 11. The P–h curve, fitting results, and corresponding stress–strain curve is shown in Fig. 12, with parameters used in the transformation process summarized in Table 3. As depicted in Fig. 12(a)–(c), the R-squared values for the Gaussian fit during the loading stage are 0.997, 0.982, and 0.994, respectively, which indicates high-quality curve fitting and confirms the reliability of the data. Consequently, the stress–strain functions for the three regions, derived from the fitting results in conjunction with the relevant formulas, are presented in Fig. 12(d)–(f).

According to the calculated results, the yield strength in region Z1 is approximately 124.6 MPa, while the yield strengths in regions Z2 and Z3 are 264.6 MPa and 636.5 MPa, respectively. The hardness-to-yield strength ratios for these regions are 2.99, 2.82, and 2.88, which aligns

with the empirical range of 2.9–3.9 obtained from Tabor's relationship [32]. This suggests that Tabor's relationship is suitable for a rough conversion between hardness and yield strength in the sintered layers when tested with a diamond Berkovich indenter. Additionally, the yield strength in Z1 is only 19.6 %–47.1 % of that in Z2 and Z3, which indicates that pressure may enhance the micromechanical properties of the sintered layers. Furthermore, the pressure-assisted region shows a yield strength deviation of approximately 58.43 %, which offers valuable data to support further investigation into the strengthening mechanisms.

4. Discussion

4.1. Influence of crystal orientation on strengthening mechanisms

The primary strengthening mechanisms in metals include dislocation strengthening, precipitation strengthening, solid solution strengthening, and grain refinement. Since the sintered silver layer is a metallic layer without precipitates, precipitation strengthening has minimal impact on its mechanical properties. In metals where non-precipitation strengthening mechanisms are dominant, the effect of texture on mechanical properties is also significant and cannot be overlooked [22].

Under applied pressure, grains often develop distinct preferred orientations, leading to anisotropy in both microstructure and micromechanical properties. Previous studies have shown that the Schmid factor acts as a link between texture and micromechanical behavior. To further examine the strengthening mechanisms of the sintered layer, calculation of the Schmid factors corresponding to the texture types shown in Fig. 8 is necessary, as outlined in Eqs. (13)–(15) [33]:

$$\cos\varphi = \frac{\vec{F}\cdot\vec{N}}{\left|\vec{F}\right|\cdot\left|\vec{N}\right|} \tag{13}$$

$$\cos\theta = \frac{\vec{F}\cdot\vec{\tau}}{\left|\vec{F}\right|\cdot\left|\vec{\tau}\right|} \tag{14}$$

$$\tau = \frac{F\cos\varphi\cos\theta}{A_0} = m\sigma \tag{15}$$

where φ represents the angle between the external force direction and the normal to the slip plane, θ is the angle between the external force direction and the slip direction, $\vec{F}$ is the direction of external force, $\vec{N}$ signifies the normal to the slip plane, $\vec{\tau}$ represents the slip direction, m is Schmid factor, τ is shear stress. According to Eq. (15), a larger Schmid factor under the same external force facilitates reaching the critical resolved shear stress, τ_{rss}, which in turn promotes slip system activation [34,35]. Given that the sintered layer is only about 15–20 μm thick along the Z-axis, forces applied during the SiC switching process mainly affect the X–Y plane. Therefore, the Schmid factors for the ideal texture of the sintered layer under various slip systems are calculated along the X and Y directions, as shown in Tables 4 and 5.

The computed results indicate that the Cube texture has a maximum Schmid factor of 0.41 in both the X and Y directions, with eight corresponding slip systems. This high susceptibility to soft orientation allows it to reach the critical shear stress first, which initiates slip. While the $Cube_{ND}$ and S textures also exhibit high maximum Schmid factor values, these correspond to only 1–2 slip systems. Deformation under external forces generally requires coordinated responses from five adjacent grains. Although the Goss texture shows a maximum Schmid factor of 0.41 in the Y direction with eight slip systems, it has only four slip systems with relatively high Schmid factor values in the X direction. The maximum Schmid factor values for the B/ $\overline{\text{B}}$ RT Cube and F textures in both the X and Y directions are 0.41. However, the corresponding slip systems are limited to only two and four groups, respectively. For both copper and RT brass textures, the maximum Schmid factor in the X direction is 0.41, with 2–4 slip systems. In contrast, the maximum Schmid factor in the Y direction is significantly lower, at 0.27, with eight active slip systems. This suggests that under localized external forces, the copper texture tends to align in a hard orientation. The RT Brass, S, and F textures exhibit relatively high strength and volume fractions in all three regions. Therefore, in the transverse comparison, the influence of these three textures on the differences in micro-mechanical properties can be considered negligible. As the volume fraction of Cube texture gradually decreases from 0.9 % (Z1) to 0.7 % (Z2) and then disappears (Z3), the hardness values progressively increase from 0.373 GPa (Z1) to 0.745 GPa (Z2), and finally reach 1.832 GPa (Z3). Additionally, the gradual development of the Copper texture and its significant increase in intensity help maintain a locally harder orientation under the applied external force.

To examine the impact of overall crystal orientation on micromechanical properties, the distribution of the maximum Schmid factor of the stress tensor along the X and Y directions is plotted and statistically analyzed using the MTEX toolbox, as shown in Fig. 13. In this plot, yellow grains represent those with a higher maximum Schmid factor, while blue grains correspond to those with a lower maximum Schmid factor.

According to the stress tensor along the X-axis, in the Z1 region, the distribution of maximum Schmid factors falls within the ranges of 0.48–0.5, 0.46–0.5, 0.44–0.5, and 0.42–0.5, with corresponding proportions of 29.56 %, 52.88 %, 71.90 %, and 83.11 %, respectively. In the Z2 region, these proportions are 28.58 %, 51.99 %, 71.97 %, and 83.81 %. In the Z3 region, the proportions are 30.06 %, 52.61 %, 71.64 %, and 83.57 %. When the applied stress tensor is oriented along the Y-axis, the maximum Schmid factor distribution in the Z1 region shows proportions of 30.29 %, 52.78 %, 71.24 %, and 82.88 % for the ranges of 0.48–0.5, 0.46–0.5, 0.44–0.5, and 0.42–0.5, respectively. In the Z2 region, these values are 29.88 %, 53.02 %, 71.46 %, and 82.59 %, while in the Z3 region, they are 29.28 %, 51.84 %, 70.76 %, and 83.05 %. Overall, it can be concluded that there are no significant differences in the distribution of the maximum Schmid factors, which do not account for the variations in micromechanical properties.

Table 4
Schmid factors of ideal textures along X direction under different slip systems.

Slip plane	(111)			$(11\bar{1})$			$(\bar{1}11)$			$(1\bar{1}1)$		
Slip direction	$[0\bar{1}1]$	$[10\bar{1}]$	$[\bar{1}10]$	$[\bar{1}10]$	$[\bar{1}0\bar{1}]$	$[0\bar{1}\bar{1}]$	$[0\bar{1}1]$	$[\bar{1}0\bar{1}]$	$[\bar{1}\bar{1}0]$	$[10\bar{1}]$	$[\bar{1}\bar{1}0]$	$[0\bar{1}\bar{1}]$
F	0	0	0	−0.41	0	0.41	0.41	0	0.41	0	0	0
B	0	0	0	0	0.27	0.27	0.41	−0.14	0.27	−0.41	0.27	−0.14
$\overline{\text{B}}$	0	0	0	−0.41	−0.14	0.27	0	0.27	0.27	0.41	−0.14	0.27
RT brass	−0.27	0.41	−0.14	−0.27	−0.27	0	0.27	0.14	0.41	0	0	0
RT cube	−0.41	0.41	0	0	−0.41	−0.41	0	0	0	0	0	0
$Cube_{ND}$	−0.49	0.16	0.33	0.33	−0.16	−0.49	−0.24	−0.08	−0.33	−0.08	0.33	0.24
S	−0.02	−0.06	−0.07	−0.26	−0.09	0.17	−0.18	0.3	0.11	0.44	−0.07	0.37
Cube	−0.41	0	0.41	0.41	0	−0.41	−0.41	0	−0.41	0	0.41	0.41
Copper	0	0	0	0	0	0	−0.41	0.41	0	0.41	0	0.41
Goss	0	0	0	0.41	0.41	0	0	0	0	−0.41	0.41	0

Table 5
Schmid factors of ideal textures along Y direction under different slip systems.

Slip plane	(111)			(11$\bar{1}$)			($\bar{1}$11)			(1$\bar{1}$1)		
Slip direction	[0$\bar{1}$1]	[10$\bar{1}$]	[$\bar{1}$10]	[$\bar{1}$10]	[$\bar{1}$01]	[01$\bar{1}$]	[0$\bar{1}$1]	[$\bar{1}$01]	[$\bar{1}\bar{1}$0]	[10$\bar{1}$]	[$\bar{1}\bar{1}$0]	[0$\bar{1}\bar{1}$]
F	0	0	0	0.41	0.27	−0.14	−0.41	0.27	−0.14	0	0.27	0.27
B	0	0	0	0	0	0	−0.41	0.41	0	0.41	0	0.41
$\bar{B}$	0	0	0	0.41	0.41	0	0	0	0	−0.41	0.41	0
RT brass	0.27	0	−0.27	0.27	0.27	0	−0.27	0.27	0	0	0	0
RT cube	0	0	0	0	0	0	−0.41	0.41	0	0.41	0	0.41
$Cube_{ND}$	0.09	0.24	−0.33	−0.33	−0.24	0.08	−0.16	0.49	0.33	0.49	−0.33	0.16
S	−0.33	0.23	0.1	0.26	0.09	−0.17	0.07	−0.01	0.06	−0.33	0.42	0.09
Cube	0	0.41	−0.41	−0.41	−0.41	0	0	0.41	0.41	0.41	−0.41	0
Copper	−0.27	0.27	0	0	0	0	0.27	0	0.27	−0.27	0.27	0
Goss	0	0.41	−0.41	−0.41	−0.41	0	0	0.41	0.41	0.41	−0.41	0

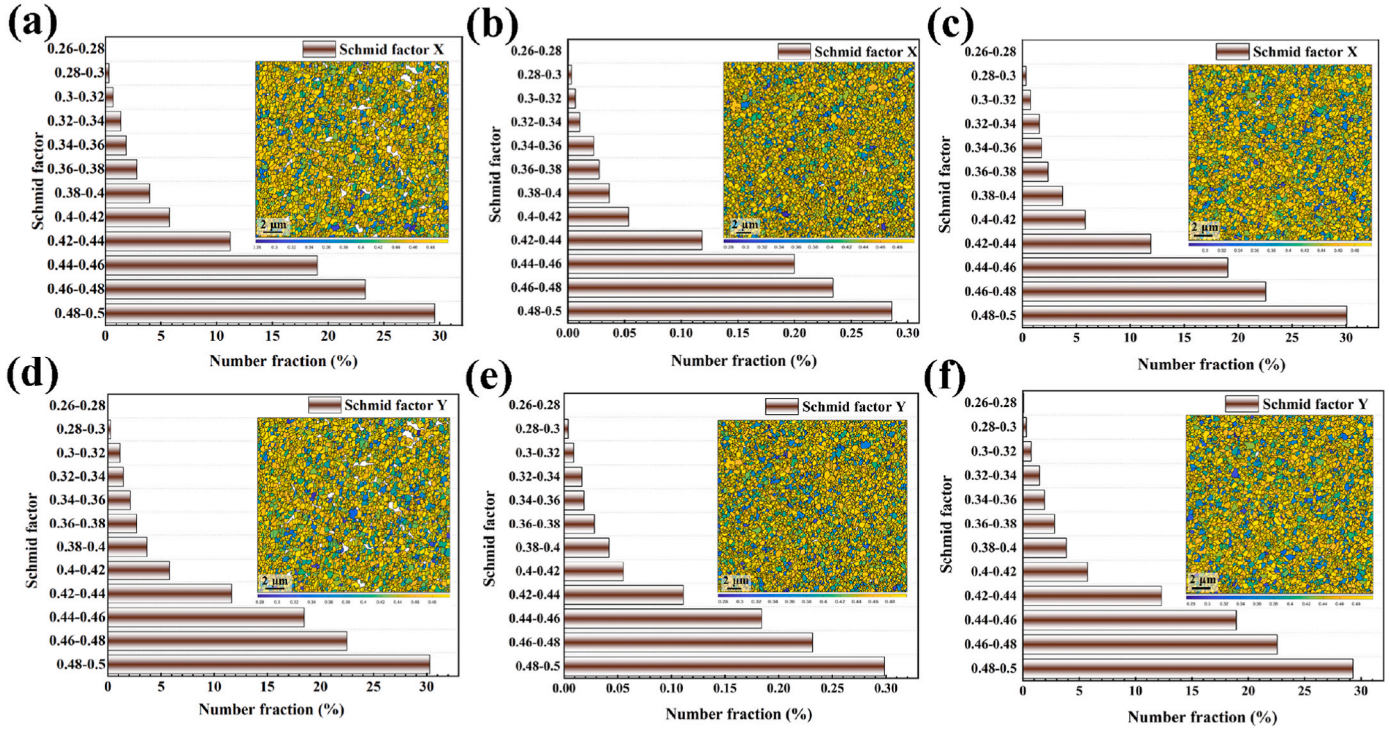

Fig. 13. The maximum Schmid factor distribution of stress tensor along the X-direction in SiC interconnect layers: (a) Z1, (b) Z2 and (c) Z3, and the maximum Schmid factor distribution of stress tensor along the Y-direction: (d) Z1, (e) Z2 and (f) Z3.

In conclusion, the gradual disappearance of the Cube texture and the emergence of the Copper texture contribute to improved micro-mechanical properties in localized regions, while the impact of the maximum Schmid factor distribution is minimal.

4.2. Influence of Hall-Petch relationship on strengthening mechanisms

Grain refinement is one of the four primary strengthening mechanisms, commonly explained by the Hall-Petch equation, which describes the relationship between grain size and yield strength. Grain boundaries impede dislocation motion, and a reduction in grain size increases the number of grain boundaries. The increase in yield strength resulting from a reduction in grain size can be calculated using the Hall-Petch relationship, as shown in Eq. (16) [36]:

$$\Delta\sigma_{H-P} = \frac{K_y}{\sqrt{D}} \tag{16}$$

where $\Delta\sigma_{H-P}$ is the yield strength increment due to grain refinement, D is the average grain size, and K_y is a material-dependent constant. Previous research shows that K_y varies across different grain size ranges. According to the results in Section 2.1.1, the grain sizes in the Z1, Z2, and Z3 regions are 0.368 μm, 0.426 μm, and 0.377 μm, respectively. Therefore, K_y can be calculated using Eq. (17) [37]:

$$K_y = M\left(\frac{Gb\tau_c}{\alpha_p}\right)^{\frac{1}{2}} \tag{17}$$

where M is the Taylor factor (commonly 3.06 for FCC metals), α_p typically takes the value of 1, and τ_c = 15–31 MPa. According to the calculations, K_y is approximately 0.0412 MPa $\sqrt{m}$. Finally, by incorporating the grain size and Hall-Petch coefficient, K_y, the yield strength increments due to grain size in the Z1, Z2, and Z3 regions are approximately 66.31 MPa, 63.12 MPa, and 67.1 MPa, respectively. These results show almost no difference in the yield strength across these three regions, with the yield strength increment in Z2 being slightly lower than that of Z1. This suggests that the difference in yield strength increment due to grain size is insufficient to explain the higher hardness and yield strength observed in the pressure-assisted zone of the sintered SiC die layer.

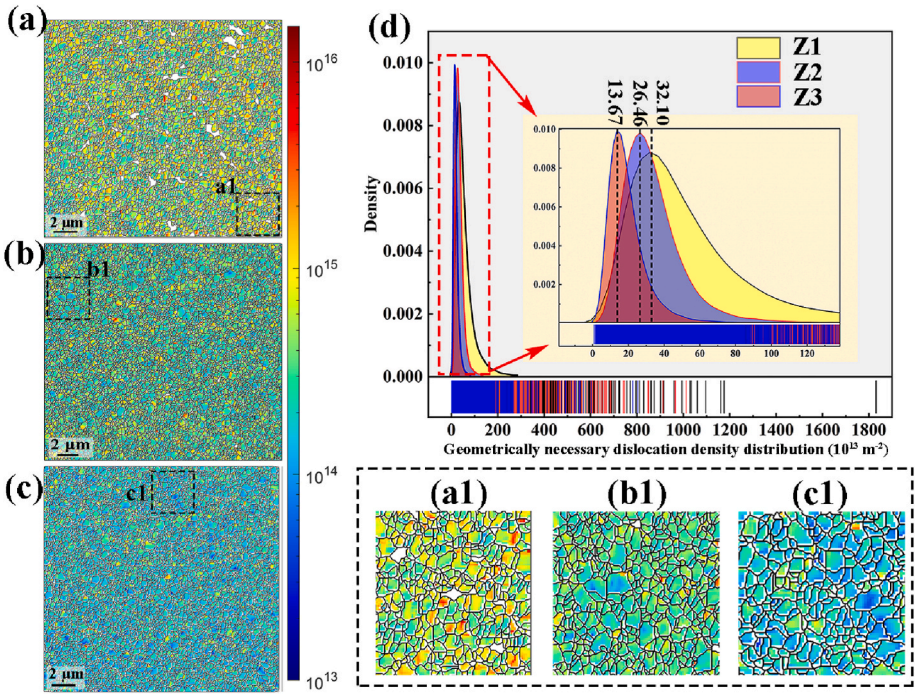

Fig. 14. GND distribution in the SiC die interconnect layer: (a) (a1) Z1, (b) (b1) Z2, and (c) (c1) Z3, and (d) statistical graph.

4.3. Influence of dislocation on strengthening mechanisms

4.3.1. Influence of GND on strengthening mechanisms

Dislocation strengthening is widely regarded as one of the most effective mechanisms among the four strengthening methods in metal materials. Previous research indicates that both SSDs and GNDs contribute equally to isotropic hardening. GNDs typically form and accumulate near grain boundaries, which increases yield strength by pinning dislocations and obstructing their motion. In contrast, SSDs predominantly develop within the grains, raise the overall dislocation density and, as a result, further enhance the material's yield strength.

In this paper, both EBSD and nanoindentation are used to differentiate the effects of GND and SSD on the micro-mechanical properties of materials. Fig. 14 illustrates the GND distribution in the interconnect layer, along with magnified views of specific regions. As shown in Fig. 14(a1)–(c1), GND tends to accumulate at grain boundaries and twin boundaries, while the GND density within the grains is generally lower than that at the boundaries. Moreover, GND density is higher in the

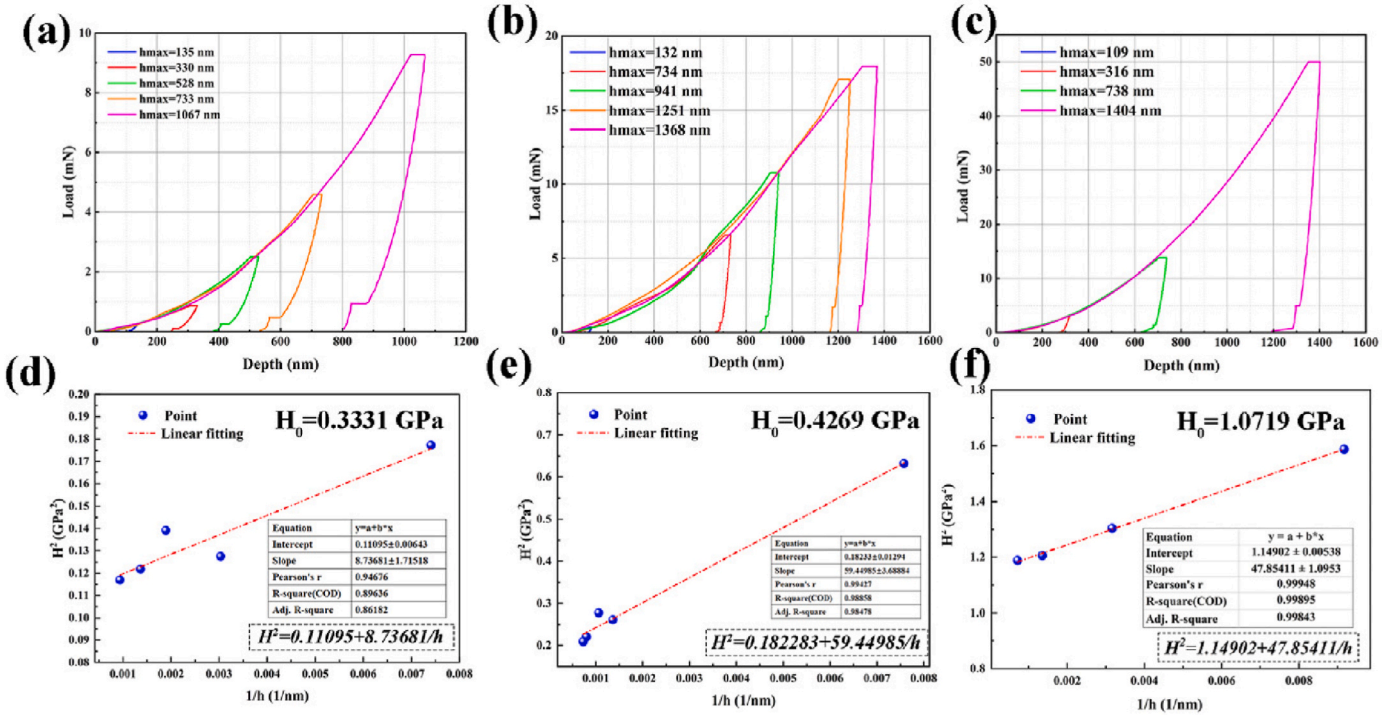

Fig. 15. P-h curves for different depths of SiC interconnect layers: (a) Z1, (b) Z2 and (c) Z3, and H^2-1/h linear fitting plot: (d) Z1, (e) Z2 and (f) Z3.

sintering pores. According to Fig. 14(a)–(d), the GND densities in the Z1, Z2, and Z3 regions are approximately 3.21 × 10^{14} m^{-2}, 2.646 × 10^{14} m^{-2}, and 1.367 × 10^{14} m^{-2}, respectively. Despite the higher GND density in the Z1 region, the hardness and yield strength are at their lowest. This suggests that GND is not the primary factor contributing to the strengthening of the sintered layers.

4.3.2. SSD calculation theory

In nanoindentation experiments, hardness typically decreases with increasing indentation depth, a phenomenon known as the indentation size effect [38]. Nix and Gao [38] demonstrated that this size effect is often associated with the presence of GND, as the indentation depth and deformation increase, which causes GND to respond to the varying strain gradient beneath the indentation. In contrast, SSD does not exhibit a size effect, which means that SSD remains unaffected by changes in indentation depth. Thus, nanoindentation is an effective method for characterizing SSD. Assuming the von Mises flow law applies, Tabor's factor (3) can be used to convert the equivalent flow stress, σ, to hardness, H, based on Eqs. (18) and (19) [38,39]:

$$H_0 = 3\sqrt{3}\alpha G b\sqrt{\rho_{SSD}} \tag{18}$$

$$H = 3\sqrt{3}\alpha G b\sqrt{\rho_{SSD} + \rho_{GND}} \tag{19}$$

where H_0 is the hardness derived from SSD, and H is the hardness measured at a specific indentation depth. Eq. (20) can be used to calculate the GND density:

$$H \Big/ H_0 = \sqrt{1 + \frac{h^*}{h}} \tag{20}$$

The indentation depth is varied to construct the H^2–$1/h$ curve and linear fitting is performed, with the intercept of the fitted line designated as H_0^2 [26,39,40]. Subsequently, the SSD can be calculated using Eq. (18).

4.3.3. Influence of SSD on strengthening mechanisms

Fig. 15 presents the P–h curves and the linear fitting of H^2–$1/h$ at various depths within the SiC interconnection layer. The R-squares of the linear fits are 0.90, 0.99, and 0.99, respectively, which indicates that the fitting results are reliable. The value of H_0 shows a gradual increase from Z1 to Z3. According to Eq. (18), the calculated SSD densities in Z1, Z2, and Z3 are 2.88 × 10^{14} m^{-2}, 4.74 × 10^{14} m^{-2}, and 2.98 × 10^{15} m^{-2}, respectively. This demonstrates a significant increasing trend, which aligns well with the observed mechanical properties. The increment in yield strength resulting from dislocation strengthening can be calculated using Eq. (21) [41]:

$$\Delta\sigma_{dis} = M\alpha G b\rho^{1/2} \tag{21}$$

where $\Delta\sigma_{dis}$ is the yield strength increment and ρ is the total dislocation density. Therefore, the yield strength increments in Z1, Z2, and Z3 are 285 MPa, 314 MPa, and 646 MPa, respectively. When considering only the influence of SSDs, the yield strength increments are 196 MPa, 251 MPa, and 620 MPa, respectively, which align more closely with the yield points observed on the stress–strain curve. It can be inferred that in the pressureless sintering region, both SSDs and GNDs significantly affect the micro-mechanical properties, where SSDs contribute approximately 69 %. However, in the pressure-assisted sintering region, SSDs exhibit a higher contribution to the micro-mechanical properties. Specifically, SSDs account for 80 % and 96 % in Z2 and Z3 regions, respectively. This indicates that the increase in strength and hardness of the die attach in the pressure-assisted sintering region primarily originates from the increase in SSDs. Therefore, SSDs are the dominant factor leading to the strengthening of the micro-mechanical properties.

In conclusion, dislocation density, particularly SSD, is the primary strengthening mechanism in sintered layers. Thus, increasing the SSD density in the sintered layer offers a promising approach to enhancing the mechanical properties of pressure-sintered materials.

4.4. Interconnect mechanism and strengthening mechanism of SiC sintered layer

Fig. 16 illustrates the interconnection and strengthening mechanisms of the SiC sintering layer. Before the sintering experiment, the organic

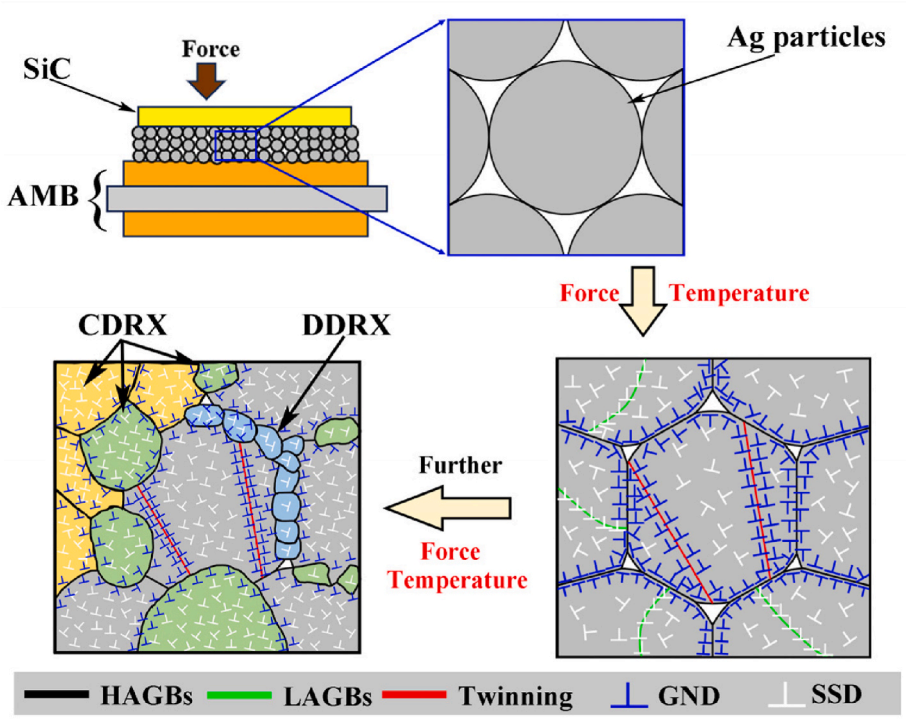

Fig. 16. Schematic diagram of interconnect and strengthening mechanisms in the sintered layer of SiC die.

components of the nano-silver paste are subjected to high-temperature drying, which results in the complete evaporation of the organic material and leaves only the nano-silver particles. Under the combined influence of temperature and pressure in the sintering device, the silver particles begin to make contact and undergo necking. During this process, GNDs accumulate at high densities around defects such as twin boundaries, HAGBs, and pores. Dislocations within the interior of the grain begin to align in an orderly arrangement and form sub-grain boundaries, as indicated by the green line in Fig. 16. With further application of pressure and temperature, the pores gradually heal through dynamic recrystallization. The sub-grain boundaries within the grains increase in misorientation under the influence of thermo-mechanical coupling. When the misorientation reaches approximately 15°, HAGBs are formed, which represents the misorientation mechanism of CDRX, as shown in the yellow grains in Fig. 16. As pressure increases, dislocations accumulate near the original grain boundaries and undergo slip and climb, which causes the initially smooth boundaries to gradually protrude. As plastic deformation progresses, the protruding regions experience lattice rotation, resulting in increased misorientation and the formation of dynamically recrystallized grains. This corresponds to the lattice rotation mechanism of CDRX, as indicated by the green grains in Fig. 16. High-density dislocations accumulate near the grain boundaries and become activated during the plastic deformation process. This phenomenon leads to the nucleation of fine recrystallized grains at the boundaries of the original large grains, resulting in the formation of fine "necklace-like" structured grains, as illustrated by the blue grains in Fig. 16. Furthermore, as the degree of recrystallization increases, GNDs near the grain boundaries (shown in blue) gradually diminish. The significant increase in SSD (shown in white) within the grains, driven by continuous and homogeneous plastic deformation, plays an increasingly important role in the dislocation strengthening of the sintered layers.

5. Conclusions

In this paper, the non-homogeneity of microstructure and micro-mechanical properties in different areas of the SiC sintered layer is mainly investigated to explore the interconnect and strengthening mechanisms. The main conclusions are as follows.

1. In the SiC sintered layers, the porosity in the Z1 is approximately 18.14 %, significantly higher than the values of 5.14 % and 3.69 % observed in the Z2 and Z3, respectively. The pressure has minimal impact on the grain size, which remains around 400 ± 50 nm. Additionally, there is no evident preferred orientation among the grains.
2. The primary interconnect mechanism of the SiC sintered layer is dynamic recovery and recrystallization, predominantly characterized by CDRX, whereas the evidence of DDRX has also been observed. Compared to the 71.7 % in the Z1, the volume fraction of recrystallized grain in the Z2 and Z3 is significantly higher, approximately 91.3 % and 89.6 %, respectively.
3. The transformation of the P–h curve into a stress–strain curve is applied to nano-silver sintered layers through mathematical modeling to obtain micro-mechanical properties. The hardness in the pressure-assisted region is approximately three times higher than in the non-pressurized region. The hardness near the SiC side is generally about 6 % lower than that near the AMB side. The hardness on the left side of the pressure-assisted sintering layer is the lowest overall and differs by approximately 21 % from the highest hardness observed in other regions. Additionally, the yield strength in the Z1 is about 124.6 MPa, which is lower than in the Z2 at 264.6 MPa and in the Z3 at 636.5 MPa. The ratio of hardness to yield strength is approximately 2.9, which is consistent with the Tabor relationship.
4. The increase in yield strength due to grain refinement is relatively minor, with a maximum difference of only about 4 MPa. The gradual disappearance of the Cube texture and the formation of the Copper texture contribute to improved micromechanical properties in localized regions, while the overall distribution of Schmid factors has minimal impact. Nanoindentation is applied to calculate SSD density for the nano-silver sintered layer through mathematical modeling for the first time, and it is found that SSD density, rather than GND density, is the most significant contributor to the enhancement of the sintered layer, providing an optimization direction for improving micromechanical properties of pressureless silver sintering.

CRediT authorship contribution statement

Chao Gu: Conceptualization, Formal analysis, Investigation, Writing – original draft, Methodology, Visualization. **Xiao Hu:** Investigation, Writing – review & editing. **Xuyang Yan:** Writing – review & editing. **Wei Chen:** Writing – review & editing. **Junwei Chen:** Writing – review & editing. **Kai Lu:** Funding acquisition, Investigation, Resources. **Tao Wang:** Funding acquisition, Investigation, Resources. **Guoqi Zhang:** Supervision. **Jiajie Fan:** Writing – review & editing, Supervision, Resources, Validation, Project administration, Funding acquisition.

Declaration of competing interest

The authors declare that they have no known competing financial interests or personal relationships that could have appeared to influence the work reported in this paper.

Acknowledgements

This work was supported by National Natural Science Foundation of China (No. 52275559).

References

[1] Tu C-C, Hung C-L, Hong K-B, Elangovan S, Yu W-C, Hsiao Y-S, et al. Industry perspective on power electronics for electric vehicles. Nat Rev Electr Eng 2024;1:435–52. https://doi.org/10.1038/s44287-024-00055-4.
[2] Wang Y, Ding Y, Yin Y. Reliability of wide band gap power electronic semiconductor and packaging: a review. Energies 2022;15. https://doi.org/10.3390/en15186670.
[3] Samavatian V, Iman-Eini H, Avenas Y, Samavatian M. Effects of creep failure mechanisms on thermomechanical reliability of solder joints in power semiconductors. IEEE Trans Power Electron 2020;35:8956–64. https://doi.org/10.1109/TPEL.2020.2973312.
[4] Paknejad SA, Mannan SH. Review of silver nanoparticle based die attach materials for high power/temperature applications. Microelectron Reliab 2017;70:1–11. https://doi.org/10.1016/j.microrel.2017.01.010.
[5] Siddiqui J, Taheri M, Alam AU, Deen MJ. Nanomaterials in smart packaging applications: a review. Small 2022;18. https://doi.org/10.1002/smll.202101171.
[6] Zhong Y, An R, Wang C, Zheng Z, Liu ZQ, Liu CH, et al. Low temperature sintering Cu6Sn5 nanoparticles for superplastic and super-uniform high temperature circuit interconnections. Small 2015;11:4097–103. https://doi.org/10.1002/smll.201500896.
[7] Yan H, Liang P, Mei Y, Feng Z. Brief review of silver sinter-bonding processing for packaging high-temperature power devices. Chinese J Electr Eng 2020;6:25–34. https://doi.org/10.23919/CJEE.2020.000016.
[8] Hong WS, Kim MS, Oh C, Joo Y, Kim Y, Hong KK. Pressureless silver sintering of silicon-carbide power modules for electric vehicles. Jom 2020;72:889–97. https://doi.org/10.1007/s11837-019-03815-y.
[9] Long X, Tang W, Xia W, Wu Y, Ren L, Yao Y. Porosity and Young's modulus of pressure-less sintered silver nanoparticles. IEEE 19th Electron Packag Technol Conf EPTC 2017 2017;2018-Febru:2017. https://doi.org/10.1109/EPTC.2017.8277577. 1–8.
[10] Yan J, Zou G, Liu L, Zhang D, Bai H, Wu A ping, et al. Sintering mechanisms and mechanical properties of joints bonded using silver nanoparticles for electronic packaging applications. Weld World 2015;59:427–32. https://doi.org/10.1007/s40194-014-0216-x.
[11] Wang C, Li G, Xu L, Li J, Zhang D, Zhao T, et al. Low temperature sintered silver nanoflake paste for power device packaging and its anisotropic sintering mechanism. ACS Appl Electron Mater 2021;3:5365–73. https://doi.org/10.1021/acsaelm.1c00857.
[12] Yeom J, Li CF, Suganuma K. Sintering mechanism of micron/submicron-size silver particles. 2018 Int Conf Electron Packag IMAPS All Asia Conf ICEP-IAAC 2018;239:121–4. https://doi.org/10.23919/ICEP.2018.8374684. 2018.
[13] Li S, Liu Y, Ye H, Liu X, Sun F, Fan X, et al. Sintering mechanism of Ag nanoparticle-nanoflake: a molecular dynamics simulation. J Mater Res Technol 2022;16:640–55. https://doi.org/10.1016/j.jmrt.2021.12.029.

[14] Hu Y, Wang Y, Yao Y. Molecular dynamics on the sintering mechanism and mechanical feature of the silver nanoparticles at different temperatures. Mater Today Commun 2023;34:105292. https://doi.org/10.1016/j.mtcomm.2022.105292.
[15] Ye G, Zhang J, Zhang P, Meng K. Sintering mechanism between silver nanoparticles and SiC/Cu plates: a molecular dynamics simulation. Powder Technol 2024;439:119695. https://doi.org/10.1016/j.powtec.2024.119695.
[16] Kostryzhev AG. Strengthening mechanisms in metallic materials. Metals (Basel) 2021;11. https://doi.org/10.3390/met11071134.
[17] Wang N, Chen Y, Wu G, Zhao Q, Zhang Z, Zhu L, et al. Non-equivalence contribution of geometrically necessary dislocation and statistically stored dislocation in work-hardened metals. Mater Sci Eng A 2022;836:142728. https://doi.org/10.1016/j.msea.2022.142728.
[18] Zhi H, Zhang C, Antonov S, Yu H, Guo T, Su Y. Investigations of dislocation-type evolution and strain hardening during mechanical twinning in Fe-22Mn-0.6C twinning-induced plasticity steel. Acta Mater 2020;195:371–82. https://doi.org/10.1016/j.actamat.2020.05.062.
[19] Kaibyshev R, Shipilova K, Musin F, Motohashi Y. Continuous dynamic recrystallization in an Al-Li-Mg-Sc alloy during equal-channel angular extrusion. Mater Sci Eng A 2005;396:341–51. https://doi.org/10.1016/j.msea.2005.01.053.
[20] Gourdet S, Montheillet F. An experimental study of the recrystallization mechanism during hot deformation of aluminium. Mater Sci Eng A 2000;283:274–88. https://doi.org/10.1016/S0921-5093(00)00733-4.
[21] Dehghan-Manshadi A, Barnett MR, Hodgson PD. Hot deformation and recrystallization of austenitic stainless steel: Part I. dynamic recrystallization. Metall Mater Trans A Phys Metall Mater Sci 2008;39(A):1359–70. https://doi.org/10.1007/s11661-008-9512-7.
[22] Momeni A, Ebrahimi GR, Jahazi M, Bocher P. Microstructure evolution at the onset of discontinuous dynamic recrystallization: a physics-based model of subgrain critical size. J Alloys Compd 2014;587:199–210. https://doi.org/10.1016/j.jallcom.2013.10.180.
[23] Cruz-Gandarilla F, Bolmaro RE, Mendoza-León HF, Salcedo-Garrido AM, Cabañas-Moreno JG. Study of recovery and first recrystallisation kinetics in CGO Fe3%Si steels using misorientation-derived parameters (EBSD). J Microsc 2019;275:133–48. https://doi.org/10.1111/jmi.12822.
[24] Kim D, Kim MS. Macroscale and microscale structural mechanisms capable of delaying the fracture of low-temperature and rapid pressureless Ag sintered electronics packaging. Mater Char 2023;198:112758. https://doi.org/10.1016/j.matchar.2023.112758.
[25] Shuman DJ, Costa ALM, Andrade MS. Calculating the elastic modulus from nanoindentation and microindentation reload curves. Mater Char 2007;58:380–9. https://doi.org/10.1016/j.matchar.2006.06.005.
[26] Luo J, Lin J. A study on the determination of plastic properties of metals by instrumented indentation using two sharp indenters. Int J Solid Struct 2007;44:5803–17. https://doi.org/10.1016/j.ijsolstr.2007.01.029.
[27] Oliver Gmp WC. An improved techniques for determining Hardness and elastic modulus using. J Mater 1992;7:1564–83.
[28] Kese KO, Li ZC, Bergman B. Method to account for true contact area in soda-lime glass during nanoindentation with the Berkovich tip. Mater Sci Eng A 2005;404:1–8. https://doi.org/10.1016/j.msea.2005.06.006.
[29] Sakharova NA, Fernandes JV, Antunes JM, Oliveira MC. Comparison between Berkovich, Vickers and conical indentation tests: a three-dimensional numerical simulation study. Int J Solid Struct 2009;46:1095–104. https://doi.org/10.1016/j.ijsolstr.2008.10.032.
[30] Bardet JP, Vardoulakis I. Use of scaling functions to determine mechanical properties of thin coatings from microindentation tests. Int J Solid Struct 2001;38:335–51. https://doi.org/10.1016/S0020-7683(00)00017-2.
[31] Dao M, Chollacoop N, Van Vliet KJ, Venkatesh TA, Suresh S. Computational modeling of the forward and reverse problems in instrumented sharp indentation. Acta Mater 2001;49:3899–918. https://doi.org/10.1016/S1359-6454(01)00295-6.
[32] Pelletier H. Predictive model to estimate the stress-strain curves of bulk metals using nanoindentation. Tribol Int 2006;39:593–606. https://doi.org/10.1016/j.triboint.2005.03.019.
[33] Bracke L, Kestens L, Penning J. Direct observation of the twinning mechanism in an austenitic Fe-Mn-C steel. Scr Mater 2009;61:220–2. https://doi.org/10.1016/j.scriptamat.2009.03.045.
[34] Zhao S, Zheng B, Zhang D, Xie X, Qu Z, Wang Y, et al. Atomistic insights into silver-indium solid solution softening mechanism for microelectronics packaging. J Mater Res Technol 2023;24:6065–75. https://doi.org/10.1016/j.jmrt.2023.04.214.
[35] Wasserbäch W, Skrotzki W, Chekhonin P. Strengthening of ods silver wires. Materialia 2020;12. https://doi.org/10.1016/j.mtla.2020.100818.
[36] Hansen N. Hall-petch relation and boundary strengthening. Scr Mater 2004;51:801–6. https://doi.org/10.1016/j.scriptamat.2004.06.002.
[37] Conrad H, Jung K. Effect of grain size from millimeters to nanometers on the flow stress and deformation kinetics of Ag. Mater Sci Eng A 2005;391:272–84. https://doi.org/10.1016/j.msea.2004.08.073.
[38] Nix WD, Gao H. Indentation size effects in crystalline materials: a law for strain gradient plasticity. J Mech Phys Solid 1998;46:411–25. https://doi.org/10.1016/S0022-5096(97)00086-0.
[39] Song E, Andani MT, Misra A. Investigation of grain size and geometrically necessary dislocation density dependence of flow stress in Mg-4Al by using nanoindentation. Acta Mater 2024;265:119633. https://doi.org/10.1016/j.actamat.2023.119633.
[40] Graça S, Colaço R, Carvalho PA, Vilar R. Determination of dislocation density from hardness measurements in metals. Mater Lett 2008;62:3812–4. https://doi.org/10.1016/j.matlet.2008.04.072.
[41] Hansen N. Boundary strengthening over five length scales. Adv Eng Mater 2005;7:815–21. https://doi.org/10.1002/adem.200500102.